

České vysoké učení technické v Praze  
Fakulta jaderná a fyzikálně inženýrská

Katedra inženýrství pevných látek  
Studijní program: Inženýrství pevných látek

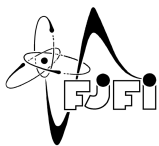


# Simulace nanoindentace pomocí molekulární dynamiky

## Simulation of the nanoindentation process using molecular dynamics

DIPLOMOVÁ PRÁCE

Vypracoval: Bc. Tibor Košťál  
Vedoucí práce: Ing. Jan Drahokoupil, Ph.D.  
Rok: 2024



**ČESKÉ VYSOKÉ UČENÍ TECHNICKÉ V PRAZE**  
**FAKULTA JADERNÁ A FYZIKÁLNĚ INŽENÝRSKÁ**  
*Katedra inženýrství pevných látek*

## **ZADÁNÍ DIPLOMOVÉ PRÁCE**

*Student:* **Bc. Tibor Košťál**

*Studijní program:* **Inženýrství pevných látek**

*Akademický rok:* **2022/2023**

*Název práce:* **Simulace nanoindentace pomocí molekulární dynamiky**  
(česky)

*Název práce:* **Simulation of the nanoindentation process using molecular dynamics**  
(anglicky)

*Pokyny pro vypracování:*

Cílem diplomové práce je nasimulovat proces nanoindentace diamantového hrotu do titanu pomocí molekulární dynamiky. Pro simulaci použijte volně dostupný program LAMMPS. Simulaci proveďte pro několik různých krystalografických orientací titanové hexagonální struktury a minimálně jeden typ hrotu. Výsledky porovnejte s dostupnými experimentálními a nasimulovanými daty.

Práce bude vypracována v anglickém jazyce.

*Doporučená literatura:*

- [1] Alexey V. Verkhovtsev, Alexander V. Yakubovich, Gennady B. Sushko, Matthias Hanauske, Andrey V. Solov'yo: *Molecular dynamics simulations of the nanoindentation process of titanium crystal*, Computational Materials Science, Volume 76, 2013, pp. 20-26.
- [2] LAMMPS, <https://www.lammps.org/index.html>
- [3] Christopher A. Schuh: *Nanoindentation studies of materials*, Materials Today, Volume 9, Issue 5, 2006, pp 32-40.
- [4] Shuai Xu, Qiang Wan, Zhendong Sha, Zishun Liu: *Molecular dynamics simulations of nano-indentation and wear of the  $\gamma$ Ti-Al alloy*, Computational Materials Science, Volume 110, 2015, pp. 247-253.

*Jméno a pracoviště vedoucího práce:*

Ing. Jan Drahokoupil, Ph.D., Katedra inženýrství pevných látek Fakulta jaderná a fyzikálně inženýrská, ČVUT v Praze.

*Jméno a pracoviště konzultanta:*

Ing. Miroslav Lebeda, Katedra inženýrství pevných látek Fakulta jaderná a fyzikálně inženýrská, ČVUT v Praze

*Datum zadání diplomové práce:* 1. 10. 2022

*Termín odevzdání diplomové práce:* 1. 8. 2023

Doba platnosti zadání je dva roky od data zadání.

.....  
*garant*

.....  
*vedoucí katedry*


.....  
*děkan*

V Praze dne 1. 10. 2022

## Prehlásenie

Prehlasujem, že som svoju diplomovú prácu vypracoval samostatne a použil som podklady (literatúru, projekty, SW atd.) uvedené v priloženom zozname.

V Prahe dňa 16.5.2024

  
.....  
Bc. Tibor Košťál

## **Podakovanie**

Rád by som poďakoval Ing. Janovi Drahekoupilovi, Ph.D. za vedenie práce a jeho cenné rady. Taktiež by som rád poďakoval Ing. Miroslavovi Lebedovi, za pomoc s programom Lammps a množstvo cenných rád. Ďalej by som chcel poďakovať katedre pevných látok za pomoc pri realizovaní práce a podpore pri štúdiu.

Bc. Tibor Košťál

*Názov práce:*

## **Simulace nanoindentace pomocí molekulární dynamiky**

*Autor:* Bc. Tibor Košťál

*Študijný program:* Inženýrství pevných látek

*Druh práce:* Diplomová práce

*Vedúci práce:* Ing. Jan Drahokoupil, Ph.D.

Katedra inženýrství pevných látek FJFI, ČVUT v Praze

*Konzultant:* Ing. Miroslav Lebeda

Katedra inženýrství pevných látek FJFI, ČVUT v Praze

*Abstrakt:* Tento výskum skúma použitie simulácií molekulárnej dynamiky na modelovanie procesov nanoindentácie. Na začiatku sa štúdia zameriava na analýzu toho, ako zmeny v rýchlosti, hĺbke a geometrii indentora ovplyvňujú správanie materiálov pod mechanickým zaťažením, pričom využíva komplexné výpočtové simulácie v programe Lammms. Skúma vplyvy rôznych tvarov a rýchlostí indentorov na charakteristiky ako tvrdosť a Youngov modul, a zisťuje, že tieto vlastnosti sú konzistentné za rôznych podmienok. Následne štúdia využíva tieto simulácie na posúdenie a porovnanie mechanických vlastností rôznych fáz a kryštálových orientácií titánu.

*Kľúčové slová:* simulácia, titan, molekulárna dynamika, nanoindentácia

*Title:*

## **Simulation of the nanoindentation process using molecular dynamics**

*Author:* Bc. Tibor Košťál

*Abstract:* This research investigates the application of molecular dynamics simulations to model nanoindentation processes. Initially, the study focuses on analyzing how variations in an indenter velocity, depth, and geometry affect the behaviour of materials under mechanical stress, using comprehensive computational simulations in the program Lammms. It examines the effects of different indenter shapes and speeds on characteristics such as hardness and Young's modulus and finds that these properties are consistent across varying conditions. Subsequently, the study employs these simulations to assess and contrast the mechanical properties of different phases and crystal orientations of titanium.

*Key words:* titanium, molecular dynamics, nanoindentation, simulations

# Contents

<b>List of Figures</b>	<b>viii</b>
<b>Introduction</b>	<b>1</b>
<b>1 Nanoindentation</b>	<b>2</b>
1.1 Materials deformation . . . . .	3
1.2 Contact mechanics . . . . .	5
1.3 Nanoindentation technique . . . . .	6
<b>2 Molecular Dynamics</b>	<b>8</b>
2.1 Basic Principles of Molecular Dynamics . . . . .	9
2.1.1 Integration of Motion . . . . .	10
2.1.2 Potential Energy Functions . . . . .	11
2.2 Tools used in molecular dynamics . . . . .	12
<b>3 Experimental methods of nanoindentation</b>	<b>14</b>
3.1 Mathematical approach and methodology . . . . .	14
3.2 Oliver-Pharr method and molecular dynamics . . . . .	17
<b>4 Simulation settings</b>	<b>19</b>
4.1 Substrate . . . . .	19
4.2 Indentor . . . . .	20
4.3 Simulation set up . . . . .	21
<b>5 Results and discussion</b>	<b>23</b>
5.1 Effect of indentation depth on simulations . . . . .	23
5.2 Analysis of simulation precision and stability . . . . .	30
5.3 Effect of indentation velocity on simulations . . . . .	32
5.4 Different indentors simulations . . . . .	34
5.5 Different crystal orientations simulations . . . . .	35
<b>Conclusion</b>	<b>37</b>
<b>Bibliography</b>	<b>39</b>
<b>Appendix</b>	<b>42</b>
A LAMMPS source code . . . . .	42

# List of Figures

1.1	Schema showing an example of practical nanoindentation. [1] . . . . .	2
1.2	Figure shows an example of stress vs strain graph, where the difference between elastic and plastic deformation can be explained. [2] . . . . .	4
1.3	. . . . .	5
1.4	Diagram shows four different shapes of indentors used during nanoindentation, a) spherical b) Conical c) Vickers d) Berkovich. [4] . . . . .	6
1.5	SEM image of a blunt Berkovich diamond nanoindenter. [5] . . . . .	7
3.1	Diagram shows an example of load-displacement data, specifying loading and unloading segments. Using the stiffness S, there can be seen the effect of the shape of the indenter. [2] . . . . .	15
3.2	Figure showing three different load-displacement graphs load vs. displacement each showing different material deformation: a) elastic deformation, b) plastic deformation and c) elastoplastic deformation. . .	16
3.3	Figure representing a cross-section of indent during nanoindentation showing all indentation depths and what depth they represent. [2] . .	16
4.1	Figure shows crystal structure of $\alpha$ and $\beta$ titanium. [15] . . . . .	19
4.2	Figure shows indentors used during simulations with different shapes: a) conical, b) cylindrical and, c) spherical. . . . .	20
4.3	Figure showing simulation set up with spherical indenter (blue), Titanium substrate (red) and fixed bottom edge (green). . . . .	21
5.1	Figure shows load-displacement data for different $h_{ind}$ as shown in the legend. The black arrow shows where the transition from elastic to plastic deformation starts. Blue and yellow arrows show atomic phenomena happening during simulations. . . . .	24
5.2	Figure shows time evolution if indenter depth for different $h_{ind}$ . . . . .	24
5.3	Figure shows load-displacement data for $h_{ind} = 20\text{\AA}$ , with dotted line showing the maximum load $P_{max}$ . The red line represents the fitted function used to calculate the stiffness of the material. . . . .	25
5.4	Figure shows the indent of simulation $h_{ind} = 10\text{\AA}$ , where we can see three layers of atoms. The blue layer is the flat surface layer, the red layer is the atoms underneath and the green layer is the atoms on the flat surface, this indicates the simulation has some indent but is small enough not to be used for analysis. . . . .	26
5.5	Figure showing the slice at $100\text{\AA}$ in the x direction with common neighbour analysis performed. Red atoms mean HCP structure as is expected and grey atoms mean without structure, which is why all surface atoms are included here. . . . .	27



5.6	Figure showing the slice at 100Å in the x direction with common neighbour analysis performed, after nanoindentation. Red atoms mean HCP structure, blue atoms represent BCC structure and grey atoms mean without structure. . . . .	27
5.7	Figure showing the slice at 100Å in the y direction with common neighbour analysis performed, after nanoindentation. Red atoms mean HCP structure, blue atoms represent BCC structure and grey atoms mean without structure. . . . .	28
5.8	Figure showing the structure of the substrate after removing HCP atoms and leaving only BCC (blue), FCC (light green) and unorganized (grey). A green circle is used to visualize how the profile of unorganized atoms looks from below. . . . .	28
5.9	The figure consists of two graphs illustrating the outcomes of the repeated simulation sets. The first graph presents load-displacement data, specifically load versus indentation depth, where all four simulations are overlaying each other. The second graph plots indentation depth against timestep, charting the progression of indentation depth and displaying the various final and maximum indentation depths observed in the simulations. . . . .	31
5.10	The figure consists of two graphs illustrating the outcomes of the second simulation sets, differentiated by various indenter velocities as indicated in the legend in the first graph. The first graph presents load-displacement data, specifically load versus indentation depth, where all five simulations are overlaying each other. The second graph plots indentation depth against timestep, charting the progression of indentation depth and displaying the various final and maximum indentation depths observed in the simulations. Arrows in the second graph represent different atomic phenomena happening in simulations, caused by atomic thermal movement. . . . .	33
11	Figure showing the first part of the code, which is divided into 5 blocks.	43
12	Figure showing the second part of the code, which is divided into 4 blocks. . . . .	44

# Introduction

Nanoindentation is a widely adopted technique in materials science for assessing a material's hardness and Young's modulus. Its popularity stems from its cost-effectiveness and the rapidity with which it can deliver results, making it an invaluable tool across various scientific fields that deal with material properties and hardness.

To enhance the cost-efficiency and depth of analysis even further, simulation has become a cornerstone of contemporary materials testing. In particular, molecular dynamics offers a detailed view of material behaviour at the atomic level, providing an intricate understanding of atomic interactions during nanoindentation tests. This simulation method was specifically selected to gain precise insights into atomic behaviour, thereby improving the accuracy of our experimental predictions.

Our research involved conducting a series of simulations that varied key nanoindentation parameters such as the indenter speed, indentation depth, and the indenter's shape. These parameters were critically examined to determine their impact on the simplicity and speed of the nanoindentation simulations. The aim was to align our results with those reported in existing literature, thereby validating our experimental approach.

For the measurement of hardness and Young's modulus, we employed the Oliver and Pharr method, a technique developed in the early 1990s that simplifies the determination of material properties. This method has been widely recognized for its efficacy and was pivotal in our analysis.

The culmination of this research involved compiling the data to select the most effective simulation parameters. Subsequently, we conducted targeted simulations on different titanium substrates, which were chosen based on their varying crystal orientations and structural characteristics. This tailored approach allowed us to better understand how different microstructural features influence material properties under nanoindentation.

# Chapter 1

## Nanoindentation

Nanoindentation, also known as depth-sensing indentation or instrumented indentation testing, is a sophisticated mechanical testing method designed to measure the mechanical properties of materials at the nanoscale. This technique is crucial for analyzing small volumes of materials, such as thin films or surface layers, where traditional testing methods fall short.

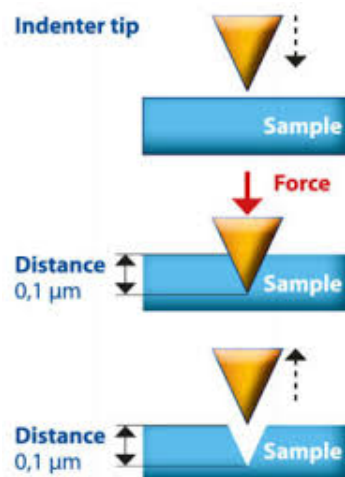


**Figure 1.1:** Schema showing an example of practical nanoindentation. [1]

In nanoindentation, a hard, sharp tip—typically made of diamond and shaped like a pyramid or cone—is pressed into the material under examination. The process involves the application of a controlled force while monitoring the penetration depth, as shown in fig. 1.1. The key parameters measured during this process are the load applied and the indenter’s displacement.

From the data gathered, several material properties can be calculated. Hardness, the elastic modulus, or Young’s modulus. The technique also assesses the creep and viscoelastic properties of the material by observing its response to a constant load over time.

Nanoindentation finds application in various fields, including materials science, engineering, and nanotechnology. It is particularly useful for characterizing coatings, thin films, and surface treatments, and for studying the mechanical properties of biological materials like bones and teeth. Additionally, it supports the development

of new materials with specific properties, such as scratch-resistant surfaces or flexible electronics, and plays a role in quality control and failure analysis in industrial processes.

The technique is highly valued for its ability to test very small sample volumes, which is beneficial for examining precious or scarce materials. Its capability to measure local properties makes it suitable for heterogeneous materials, such as composites or materials with varying phases. Furthermore, its high spatial resolution enables the study of micro-structural features like grain boundaries and phase interfaces, making nanoindentation a vital tool in material science for uncovering detailed insights into material behaviour at microscopic scales.

## 1.1 Materials deformation

As mentioned in the previous section, nanoindentation is based on the indent created by indenter, also called deformation. This deformation can be used to determine hardness or any other material parameters. There are different deformations but the main two categories are elastic and plastic types, which involve understanding the concepts of stress and strain, along with the mechanical property known as Young's modulus. Stress is the internal force per unit area within a material that arises due to externally applied forces. It is essentially how much force the material is experiencing per unit of its cross-sectional area. The standard formula for calculating stress ( $\sigma$ ) is

$$\sigma = \frac{F}{A} \quad (1.1)$$

where  $F$  is the applied force and  $A$  is the area over which the force is distributed. Stress is measured in units like Pascals (Pa). Strain is the measure of the deformation or change in shape that a material undergoes due to the applied stress. It represents the relative change in length or size and is expressed as a ratio of the change in dimension to the original dimension. The formula for strain  $\epsilon$  is

$$\epsilon = \frac{\Delta L}{L} \quad (1.2)$$

where  $\Delta L$  is the change in length and  $L$  is the original length. Strain is dimensionless since it's a ratio. Stress and strain describe how materials respond to applied forces, which is crucial for designing and assessing the strength and durability of structures and products.

Young's Modulus (Elastic Modulus) quantifies the stiffness of an elastic material and is defined as the ratio of tensile stress  $\sigma$  to tensile strain  $\epsilon$ , applicable in the elastic deformation conditions. The relationship is expressed mathematically as:

$$E = \frac{\sigma}{\epsilon} \quad (1.3)$$

Elastic Deformation occurs when the material returns to its original shape and size after the removal of the applied stress, characterizing this deformation as reversible. Within the elastic limit, this behaviour follows Hooke's Law, which states:

$$\sigma = E\epsilon \quad (1.4)$$

Here, the stress is proportional to the strain up to the yield strength of the material, which marks the commencement of plastic deformation. Plastic Deformation results in permanent changes in the material when stress exceeds the yield strength. Unlike elastic deformation, plastic deformation does not revert even after the stress is removed. Beyond the yield point, the stress-strain relationship ceases to be linear and Hooke's Law no longer holds.

The stress-strain curve provides a graphical representation of the material's response to loading. The initial slope of this curve, corresponding to Young's modulus, represents the elastic behaviour. The curve's progression beyond the yield point, where it flattens or ascends at a reduced slope, indicates the plastic phase of deformation.

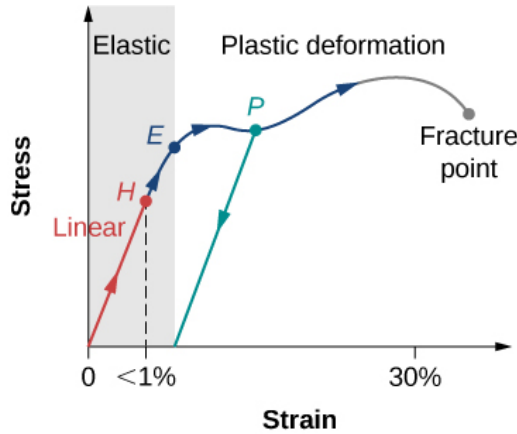


**Figure 1.2:** Figure shows an example of stress vs strain graph, where the difference between elastic and plastic deformation can be explained. [2]

Understanding these transitions between elastic and plastic deformation through Young's modulus is crucial for predicting how materials behave under different loading conditions, critical in engineering and construction to select materials based on their stress-resistance characteristics. Both of these deformations can be shown in the stress-strain graph shown in fig. 1.2.

Another material property calculated from nanoindentation, as mentioned in the previous section, is hardness. In nanoindentation testing, hardness  $H$  is an essential mechanical property that quantifies a material's resistance to deformation under an applied force. The hardness is mathematically defined by the equation

$$H = \frac{P_{\max}}{A} \quad (1.5)$$

where  $P_{\max}$  represents the maximum load applied during the testing, and  $A$  is the contact area of the indentation [2]. The contact area  $A$  is influenced by the geometry of the indenter and the depth of indentation, which are crucial for accurately

calculating hardness. This equation illustrates that the hardness value increases as either the load  $P_{\max}$  for a given contact area  $A$  increases, or as the indentation area  $A$  decreases for a given load. This relationship is pivotal in assessing the structural integrity and durability of materials; higher hardness values generally indicate better material performance under stress. Thus, hardness testing is vital in material optimization for applications demanding high strength and wear resistance, such as coatings and structural components.

## 1.2 Contact mechanics

This section describes into elastic and elasto-plastic contact and how it relates to nanoindentation techniques and extracting hardness and Young's modulus values. The contact between the indenter and specimen is in particular interest for studying nanoindentation. The most well-known example is contact between the spherical indenter and specimen, as shown in fig. 1.3.

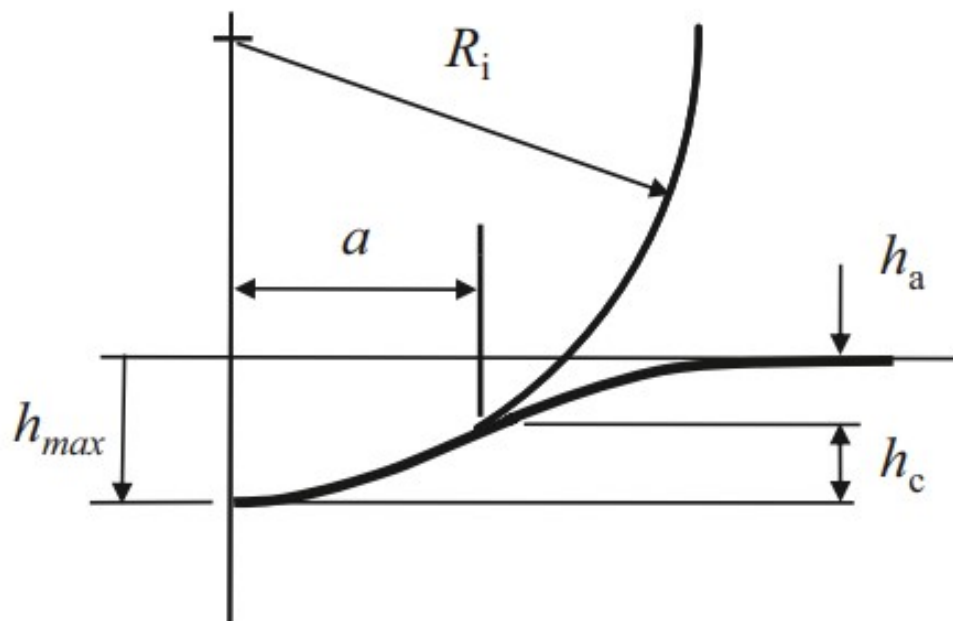


**Figure 1.3**

Hertz's theory for elastic contact [3] states that the constant circle radius  $a$ , indentation load  $P$ , indenter radius  $R$  and elastic properties of contacting materials are related and can be given the form of

$$a^3 = \frac{3PR}{4E^*} \quad (1.6)$$

where the  $E^*$  combines the modulus of the indenter and the specimen, this is given and combined in eq. 1.7, where the  $E^*$  is referred often as combined modulus.

$$\frac{1}{E^*} = \frac{1 - \nu^2}{E} + \frac{1 - \nu'^2}{E'} \quad (1.7)$$

The stated  $R$  in eq. 1.7 is set to be always positive and can be defined as eq. 1.8, if both contacting bodies have a curvature. Using the Hertz theory, which also takes into account that the deformations are localized not the bulk deformations, which defines deflection of the original surface connection between different indentation depths can be made as  $h_a = h_c = h_{max}$

$$\frac{1}{R} = \frac{1}{R_1} + \frac{1}{R_2} \quad (1.8)$$

Using the non-rigidnes of indenter and equations of contact pressure mentioned in [4],  $E^*$  can be written as

$$E^* = \frac{1}{2} \frac{dP}{dh} \frac{\sqrt{\pi}}{\sqrt{A}} \quad (1.9)$$

### 1.3 Nanoindentation technique

The ambition of nanoindentation is to measure hardness and Young's module of the tested specimen. Conventional testing involves using the geometry of the indenter and measuring the plastic indent itself. This provides the measured data necessary for later analysis. The indent itself is only a few microns across and it makes it hard to determine its geometry using conventional optical techniques. The known

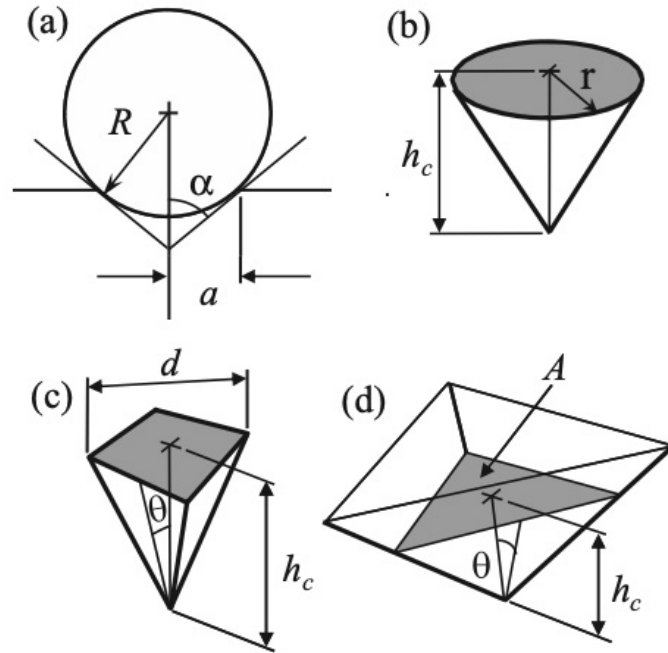


**Figure 1.4:** Diagram shows four different shapes of indentors used during nanoindentation, a) spherical b) Conical c) Vickers d) Berchovich. [4]

geometry then allows the size of the contact area to be determined. This effect is also affected when the shape of an indenter is chosen.

There are multiple indenter types practically used in nanoindentation and one of the most important is the type of indenter used. There are four main types of indentors: spherical, conical, Vickers and Berkovich. All of these can be seen in fig. 1.4. Spherical indentors are finding more popularity in applications because of their smooth transition from elastic to elastic-plastic deformations [4]. Fig. 1.4 shows the types of indenter but what is important to mention, from an anatomical point of view the indentors used are blunt. This can be seen in the fig. 1.5 which shows the SEM (Scanning electron microscope) image of the Berkovich indenter.

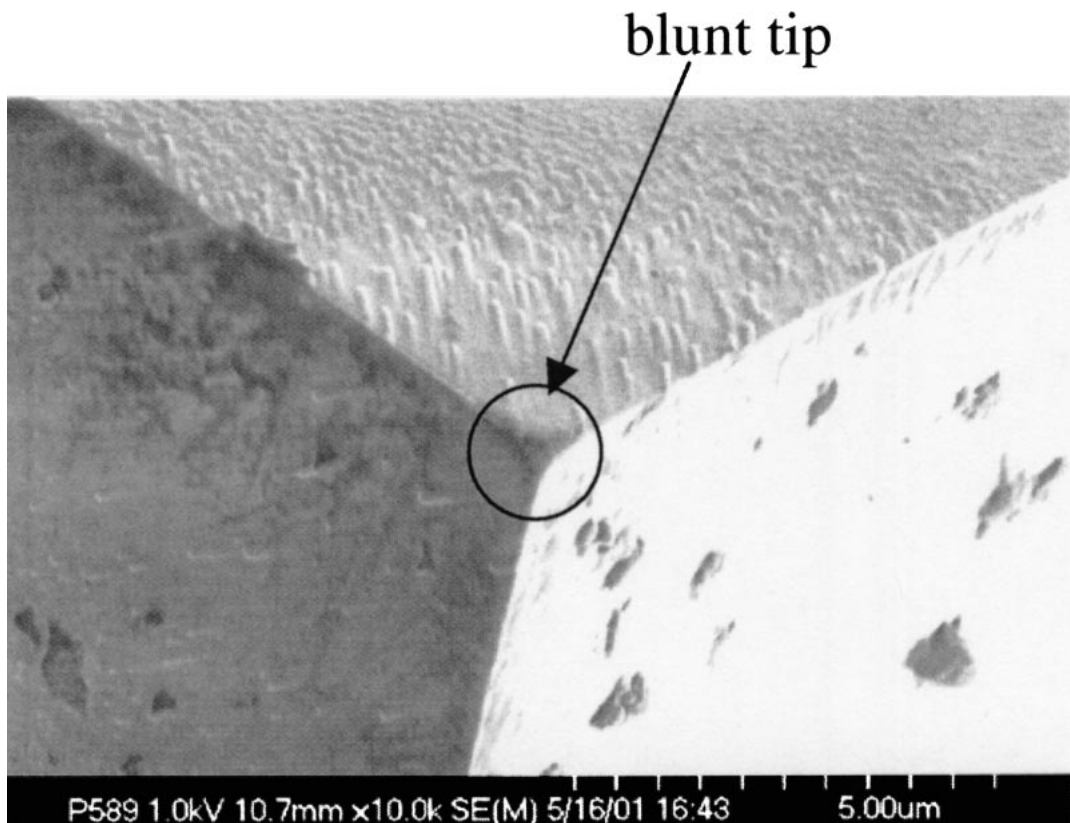


**Figure 1.5:** SEM image of a blunt Berkovich diamond nanoindenter. [5]



# Chapter 2

## Molecular Dynamics

Molecular dynamics (MD) is a computational simulation technique used in various scientific disciplines to study the dynamic behaviour of molecular systems over time. It provides insights into the movement and interactions of atoms and molecules by numerically solving the classical equations of motion. The primary goal of molecular dynamics is to simulate the temporal evolution of a molecular system under the influence of interatomic forces, allowing researchers to observe and analyze its behaviour at the atomic and molecular levels [6].

Key components of molecular dynamics simulations include:

- **Force Fields:** MD simulations rely on mathematical models known as force fields, which describe the potential energy surfaces and forces acting between atoms and molecules. Force fields include parameters for bond lengths, angles, and non-bonded interactions (such as van der Waals forces and electrostatic interactions).
- **Integration Algorithms:** To calculate the trajectory of a molecular system over time, numerical integration algorithms are employed to solve the equations of motion. Common algorithms include the Verlet algorithm and the leapfrog integrator, among others.
- **Initial Conditions:** MD simulations require an initial set of atomic coordinates and velocities. These initial conditions, often derived from experimental data or previous simulations, determine the starting configuration of the molecular system.
- **Ensemble and Temperature Control:** MD simulations can be conducted under various thermodynamic ensembles, such as the NVE (constant number of particles, volume, and energy), NVT (constant number of particles, volume, and temperature), or NPT (constant number of particles, pressure, and temperature). Temperature control is achieved through algorithms that adjust particle velocities to maintain the desired temperature.
- **Boundary Conditions:** Simulations are often conducted in periodic boundary conditions, allowing researchers to study representative parts of a system while minimizing edge effects. This involves creating artificial replicas of the simulation box to account for interactions beyond the primary simulation cell.

Molecular dynamics has applications in a wide range of scientific fields, including chemistry, biochemistry, physics, materials science, and drug discovery. Researchers use MD simulations to investigate phenomena such as protein folding, chemical reactions, phase transitions, and the mechanical properties of materials. The ability to observe molecular motion at the atomic level provides valuable insights that complement experimental observations and aid in the understanding of complex systems.

## 2.1 Basic Principles of Molecular Dynamics

MD method observes the evolution of a system composed of atoms/molecules in real time. Classical MD consider an atomic system with an initial state defined by specifying the positions  $\mathbf{r}_i$  and velocities  $\mathbf{v}_i$  of all particles in the system. Additionally, the types of particles and their interactions are defined through potential energy functions [7].

In molecular dynamics simulations, the forces exerted on each particle are critical for determining how the particles move over time. These forces are derived from the potential energy of the system, which is a function of the positions of all particles. The force on the  $i$ -th particle, denoted as  $\mathbf{F}_i$ , can be calculated by taking the negative gradient of the potential energy function ( $U$ ) with respect to the position of the particle ( $\mathbf{r}_i$ ):

$$\mathbf{F}_i = -\nabla U(\mathbf{r}_1, \mathbf{r}_2, \dots, \mathbf{r}_N) = -\frac{\partial U}{\partial \mathbf{r}_i}, \quad (2.1)$$

where  $\mathbf{r}_1, \mathbf{r}_2, \dots, \mathbf{r}_N$  represent the positions of all  $N$  particles in the system [7].

The potential energy  $U$  is a sum of different components, each corresponding to various types of interactions between particles. These can be broadly categorized into bonded and non-bonded interactions:

$$U = U_{\text{bonded}} + U_{\text{non-bonded}}, \quad (2.2)$$

where  $U_{\text{bonded}}$  includes terms for chemical bonds, angles, and dihedrals, and  $U_{\text{non-bonded}}$  includes terms for van der Waals and electrostatic interactions.

### Non-bonded Interactions

Non-bonded interactions are typically the most computationally demanding part of force calculations due to the need to consider every pair of particles in the system. The Lennard-Jones potential is commonly used to model van der Waals forces, while electrostatic forces are calculated using the Coulomb's law:

$$U_{\text{LJ}}(r_{ij}) = 4\epsilon \left[ \left( \frac{\sigma}{r_{ij}} \right)^{12} - \left( \frac{\sigma}{r_{ij}} \right)^6 \right], \quad (2.3)$$

$$U_{\text{Coulomb}}(r_{ij}) = \frac{1}{4\pi\epsilon_0} \frac{q_i q_j}{r_{ij}}, \quad (2.4)$$

where  $r_{ij}$  is the distance between particles  $i$  and  $j$ ,  $\epsilon$  and  $\sigma$  are parameters of the Lennard-Jones potential,  $q_i$  and  $q_j$  are the charges of the particles, and  $\epsilon_0$  is the vacuum permittivity.

## Bonded Interactions

Bonded interactions include forces due to chemical bonds, bond angles, and torsional angles. These are typically modelled using harmonic potentials or more complex functions that take into account the geometry of the molecule:

$$U_{\text{bond}} = \frac{1}{2} k_{\text{bond}} (r - r_0)^2, \quad (2.5)$$

$$U_{\text{angle}} = \frac{1}{2} k_{\text{angle}} (\theta - \theta_0)^2, \quad (2.6)$$

$$U_{\text{dihedral}} = \sum_n k_{\text{dihedral},n} (1 + \cos(n\phi - \delta)), \quad (2.7)$$

where  $k_{\text{bond}}$  and  $k_{\text{angle}}$  are force constants for bonds and angles,  $r$  and  $\theta$  are the current bond length and angle,  $r_0$  and  $\theta_0$  are their equilibrium values, and  $k_{\text{dihedral},n}$ ,  $n$ , and  $\delta$  are parameters defining the torsional potential [7].

The calculation of forces is thus a direct consequence of these potential energy functions, and it is these forces that drive the dynamics of the system in a molecular dynamics simulation.

### 2.1.1 Integration of Motion

The core of molecular dynamics simulations lies in the numerical integration of Newton's equations of motion. This process updates the positions and velocities of all particles in the system over time, based on the forces calculated from the potential energy surface. Given the acceleration  $\mathbf{a}_i$  of particle  $i$ , which is obtained from the force  $\mathbf{F}_i$  as  $\mathbf{a}_i = \mathbf{F}_i/m_i$ , where  $m_i$  is the mass of the particle, the goal is to solve the second-order differential equation:

$$m_i \frac{d^2 \mathbf{r}_i}{dt^2} = \mathbf{F}_i. \quad (2.8)$$

Numerical integration algorithms, such as the Verlet algorithm and its variants, are commonly used to achieve this. The Velocity Verlet algorithm, in particular, is widely used due to its simplicity and good balance of accuracy and computational efficiency. The Velocity Verlet algorithm updates the positions and velocities of particles using the following equations:

$$\mathbf{r}_i(t + \Delta t) = \mathbf{r}_i(t) + \mathbf{v}_i(t)\Delta t + \frac{1}{2}\mathbf{a}_i(t)\Delta t^2, \quad (2.9)$$

$$\mathbf{v}_i(t + \Delta t) = \mathbf{v}_i(t) + \frac{1}{2}[\mathbf{a}_i(t) + \mathbf{a}_i(t + \Delta t)] \Delta t, \quad (2.10)$$

where  $\Delta t$  is the time step,  $\mathbf{r}_i(t)$  and  $\mathbf{v}_i(t)$  are the position and velocity of particle  $i$  at time  $t$ , respectively, and  $\mathbf{a}_i(t)$  is the acceleration of particle  $i$  at time  $t$ .

The choice of time step  $\Delta t$  is critical for the accuracy and stability of the simulation. A too-large time step can lead to inaccurate results or numerical instability, while a too-small time step increases computational costs without significant gains in accuracy [7].

## 2.1.2 Potential Energy Functions

Potential energy functions, or potentials, describe the energy of a system as a function of the positions of its particles. These functions are central to molecular dynamics simulations because they determine the forces exerted on the particles. Two important classes of potential energy functions are the Lennard-Jones (LJ) potential, which models non-bonded interactions, and the Modified Embedded Atom Method (MEAM) potentials, which provide a more complex description of metallic bonds.

### Lennard-Jones Potential

The Lennard-Jones potential is one of the simplest and most widely used models for the interaction between a pair of neutral atoms or molecules. It captures the essence of the van der Waals forces, including both the attractive and repulsive components, as a function of the distance between the particles. The potential is given by:

$$U_{\text{LJ}}(r) = 4\epsilon \left[ \left( \frac{\sigma}{r} \right)^{12} - \left( \frac{\sigma}{r} \right)^6 \right], \quad (2.11)$$

where:

- $r$  is the distance between the centres of two particles,
- $\epsilon$  is the depth of the potential well, representing the strength of the attraction,
- $\sigma$  is the distance at which the potential is zero, representing the effective diameter of the particles.

The  $r^{-12}$  term describes the repulsive forces at short ranges (due to electron cloud overlap), while the  $r^{-6}$  term accounts for the attractive forces at longer ranges (dispersion forces). The Lennard-Jones potential is particularly useful for simulations involving nonpolar molecules and noble gases [8].

## Modified Embedded Atom Method (MEAM) Potentials

The Modified Embedded Atom Method (MEAM) is an extension of the Embedded Atom Method (EAM), both of which are used to model metallic bonding with greater accuracy than pair potential models like the Lennard-Jones potential. MEAM incorporates angular dependency and modifications to better account for the directional characteristics of metallic bonds, making it suitable for simulating a wider range of materials, including alloys and transition metals.

The MEAM potential energy of an atom in a metal is formulated as a function of its local environment, including both the electron density contributed by neighbouring atoms and the geometric configuration of those neighbours. The total potential energy of a system in the MEAM framework can be expressed as:

$$U_{\text{MEAM}} = \sum_i F(\rho_i) + \frac{1}{2} \sum_{i \neq j} \phi(r_{ij}) + \text{angular terms}, \quad (2.12)$$

where:

- $F(\rho_i)$  is the embedding energy function, depending on the local electron density  $\rho_i$  at atom  $i$ ,
- $\phi(r_{ij})$  is a pairwise potential function, similar to the pair potentials but modified to include the effects of electron density,
- The angular terms account for the influence of the angles between bonds on the potential energy, enhancing the model's ability to simulate complex structures and defects.

MEAM potentials provide a more comprehensive description of the interactions in metallic systems, capturing not only the effect of atomic distances but also the arrangement of atoms, thereby enabling more accurate simulations of mechanical properties, phase transitions, and other phenomena in metals and alloys [9].

In summary, the choice of potential energy function plays a crucial role in the accuracy and applicability of molecular dynamics simulations. While the Lennard-Jones potential is suitable for simple molecular or noble gas systems, MEAM potentials offer a more detailed model for the complex interactions in metallic materials.

## 2.2 Tools used in molecular dynamics

Among the notable molecular dynamics simulation software, LAMMPS, GROMACS, and NAMD each offer unique capabilities and specializations.

LAMMPS is a highly versatile and widely used software for simulating particles at atomic to continuum scales across various fields such as physics, materials science, chemistry, and biology. It excels in handling large-scale simulations efficiently thanks to its parallel computing capabilities. The software supports a variety of interaction styles and force fields, and its high customizability allows users to integrate new functionalities as needed.

GROMACS, originally designed for simulating biochemical molecules like proteins, lipids, and nucleic acids, is also adept at handling non-biological systems. Known for its speed and efficiency on both CPUs and GPUs, GROMACS supports an extensive range of force fields and provides comprehensive tools for simulation setup, execution, and analysis. This makes it particularly suitable for studies involving large biomolecular complexes.

NAMD, developed for high-performance simulation of large biomolecular systems, stands out for its ability to scale efficiently across many nodes in high-performance computing environments. It integrates closely with the visualization tool VMD, enhancing the user's ability to analyze complex molecular interactions. Supporting various force fields and advanced sampling techniques, NAMD is a preferred tool for researchers in biophysics.

Each tool is tailored to specific needs within the molecular dynamics field, providing robust solutions for both academic and industrial research. LAMMPS's customizability makes it suitable for a broad range of applications, GROMACS is optimized for speed in complex biological systems, and NAMD offers excellent scalability for detailed biophysical studies.

# Chapter 3

## Experimental methods of nanoindentation

There are many techniques and methods used to determine the material's hardness and Young's module. One of the most used methods is the Oliver-Pharr method (O&P) introduced in 1992. Oliver and Pharr took and improved upon the work of Doerner and Nix (D&N), which advanced the field of materials science with their pioneering work on nanoindentation, particularly through their 1986 study that developed methods to accurately measure the mechanical properties of thin films. They introduced a model to correct substrate effects in nanoindentation measurements, enabling more precise determination of thin film properties independent of their substrates. In the Oliver-Pharr method, the projected contact area between the indenter tip and material is estimated using the equations for the elastic contact of an indenter of arbitrary shape on a uniform and isotropic half-space [2]. The indentation modulus and hardness of the material can thus be calculated without the necessity of imaging the indentation after the experiment.

### 3.1 Mathematical approach and methodology

O&P's approach involves recording and analyzing both the loading and unloading curves during the indentation process, called load-displacement data shown in fig. 3.1. During the loading phase, a predetermined force is applied to the material via a diamond indenter, and the depth of penetration is measured. The unloading phase, where the force is gradually withdrawn, is particularly critical for this method; the shape of the unloading curve provides essential information about the material's elastic properties. By examining the slope at the onset of the unloading curve, Oliver and Pharr devised a way to more accurately calculate the contact stiffness, a key parameter for determining the material's elastic modulus. This improved understanding of the mechanical response under indentation not only offers precise measurements of stiffness and hardness but also allows for a deeper insight into the material's structural integrity and deformation behaviours.

Load-displacement data are core aspects of O&P's approach for nanoindentation. The equation for many simple punch geometries according to [2] can be written as

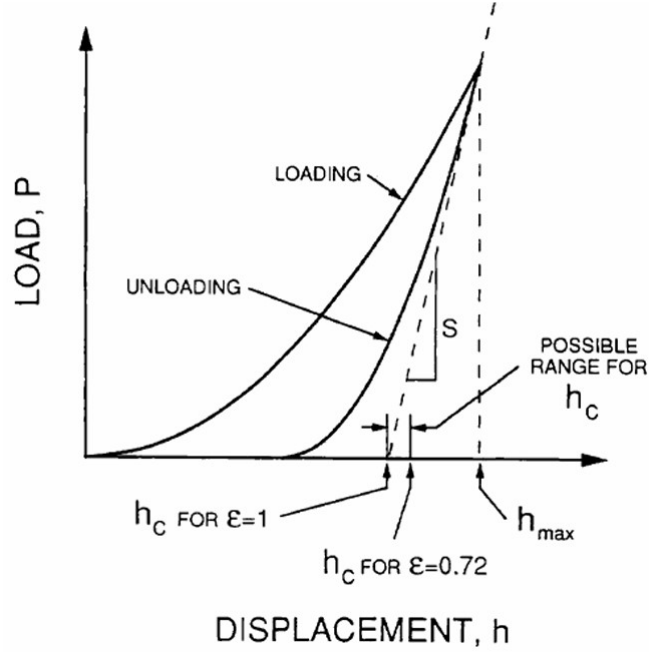


**Figure 3.1:** Diagram shows an example of load-displacement data, specifying loading and unloading segments. Using the stiffness  $S$ , there can be seen the effect of the shape of the indenter. [2]

$$P = \alpha h^m \quad (3.1)$$

where  $P$  is the indenter load,  $h$  is the elastic displacement of the indenter, and  $\alpha$  and  $m$  are constants. Values for these exponents are  $m = 1$  for flat cylinders,  $m = 2$  for cones,  $m = 1.5$  for spheres in the limit of small displacements, and  $m = 1.5$  for paraboloids.

As mentioned in chap. 1, there are two different deformations elastic and plastic deformation. In the nanoindentation, there is also elastoplastic or inelastic, which is specific for nanoindentation. These different types of deformations can also be seen using load-displacement curves. Fig. 3.2 represent three different types of load-displacement curves and it shows three different deformations based also on the equation used to describe these load-displacement curves. O&P's approach defines the general equation for load-displacement data as 3.1, but specifically for loading and unloading curves are specified as

$$P = \alpha_1 h^m \quad \text{and} \quad P = \alpha_2 (h - h_f)^m \quad (3.2)$$

where  $h_f$  is the final indentation depth.

Coming back to elastic displacement  $h$ , using fig. 3.3 displaying the profile of an indent, elastic displacement can be also called the final indentation depth  $h_f$ , is defined as

$$h = h_c + h_s \quad (3.3)$$



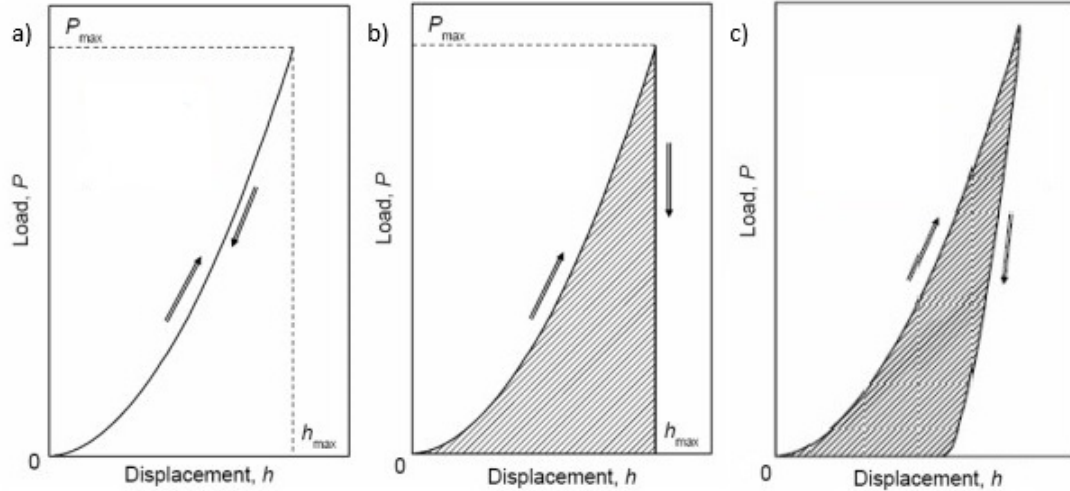


**Figure 3.2:** Figure showing three different load-displacement graphs load vs. displacement each showing different material deformation: a) elastic deformation, b) plastic deformation and c) elastoplastic deformation.

where  $h_c$  is the contact depth or the distance under which indenter tip contact is made normal to the sample surface, and  $h_s$  represents the surface displacement (which is now classified in the literature as pile-up, sink-in, or both, depending upon the material deformation mechanics, among other factors) about the contact perimeter. This is the main idea taken from O&P's method, which uses this definition of  $h_f$  to calculate hardness and Young's module. O&P's method is also based on Hertz's theory for elastic contact [3], which states that the stiffness is defined as

$$S = \frac{dP}{dh} \quad (3.4)$$

of the contact between two elastic spheres, where  $P$  is the contact force, and  $h$  is the relative movement of the centres of the spheres. Elastic contact is defined by Hertz's theory and contact mechanic using the eq. 1.9 as

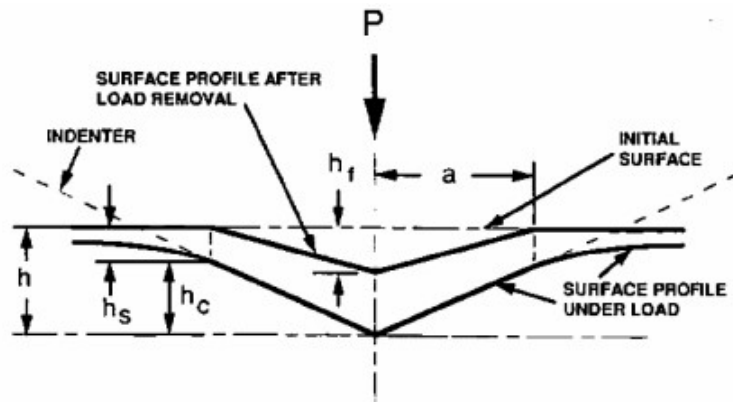


**Figure 3.3:** Figure representing a cross-section of indent during nanoindentation showing all indentation depths and what depth they represent. [2]

$$E_r = \frac{\sqrt{\pi}}{2\sqrt{A_C}} S \quad (3.5)$$

where  $E_r$  is defined as

$$\frac{1}{E_r} = \frac{1 - \nu^2}{E} + \frac{1 - \nu^2}{E_i} \quad (3.6)$$

is an effective elastic modulus of the two spheres,  $E_1$  and  $E_2$  are their Young's module,  $\nu_1$  and  $\nu_2$  their Poisson's ratio and  $A_C$  is the projected area of contact. Sneddon has shown that eq. (3.6) holds for other shapes, e.g. cones, pyramids, and a flat punch on a flat surface [10].

Using these equations we can determine the slope of the unloading curve which gives value for stiffness as mentioned in (3.4). This is one of the many advantages of using the O&P's approach since there are theoretically no needed measurements of the indent to determine the hardness.

As was mentioned in chap. 1, the hardness can be calculated with

$$H = \frac{P_{\max}}{A} \quad (3.7)$$

where  $P_{\max}$  is maximum load and  $A$  is a contact surface. Problematic with using this equation is determining the contact area during nanoindentation. As is shown in the fig. ??, there is clear difference between contact depth  $h_c$ , final depth  $h_f$  and total depth  $h$ , as mentioned in (3.3). Considering O&P's theory states that contact depth can be calculated using this equation

$$h_c = h_f - h_s \quad (3.8)$$

where  $h_s$  is called the elastic deflection of the surface and can be calculated from elastic contact using

$$h_s = \epsilon \frac{P_{\max}}{S} \quad (3.9)$$

In the eq. 3.9,  $\epsilon$  is the indentation load and is a constant that depends only on the shape of the indenter,  $\epsilon = 0.72$  for a conical tip and  $0.75$  for a paraboloid tip [1]. Once  $h_s$  has been calculated, the projected contact area,  $A$ , can be determined from the shape of the indenter. Once the contact area is known, the indentation modulus and hardness of the material are readily calculated.

## 3.2 Oliver-Pharr method and molecular dynamics

When working with nanonidnentaion, there needs to e clear separation between the laboratory experiments and Md simulations. One of the biggest difference is the scale of the substrate, since MD simulations are working on atomic scales, the size

of the simulation cant reach the length to be the same as a laboratory experiment. On the other hand this is the advantage of the MD simulation compared to the real experiments since atomic behavior can be observed during nanoindentaion.

O&P's approach is experimental approach but when closely examined it can be applied also to simulation approach since the requirement are only the load-displacement data and indenter parameter. All these can be calculated and used from simulations.

# Chapter 4

## Simulation settings

During this work "Large-scale atomic-molecular massively parallel simulator" (LAMMPS) [11] was used to perform a series of MD simulations. As complementary software OVITO [12] and AtomsK [13] were used for visualization and structure generation.

### 4.1 Substrate

The material chosen for simulations is titanium. Generally, pure titanium can crystallize in two crystal structures:  $\alpha$  titanium and  $\beta$  titanium. When it crystallizes at low temperatures (room temperature), the hexagonal close-packed (HCP) structure of alpha titanium is formed. Both structures were chosen for the final simulation and for  $\alpha$  titanium three different crystal orientations ( $\langle 100 \rangle$ ,  $\langle 110 \rangle$  and  $\langle 111 \rangle$ ) from [14] were chosen to see the effect of crystal orientation on hardness and Young's module.

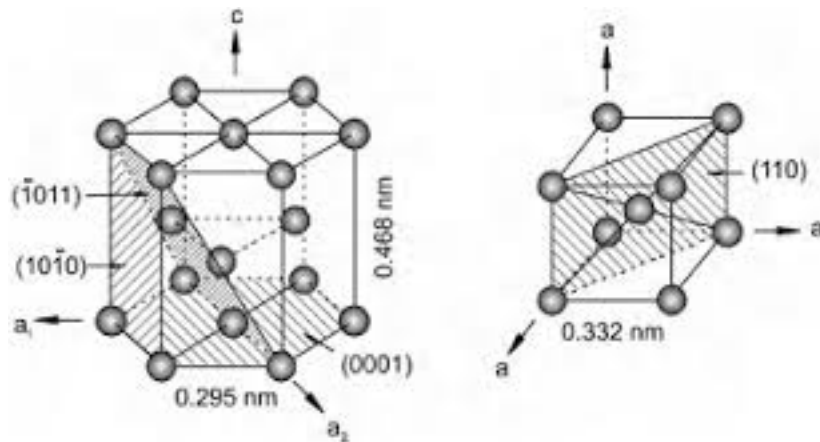


**Figure 4.1:** Figure shows crystal structure of  $\alpha$  and  $\beta$  titanium. [15]

Simulations required to run nanoindentation calculations using MD are joined with a couple of challenges. The first challenge is connected with a number of atoms vs. computational time. Since with more atoms comes also more time to compute any simulation. Modelling of the substrate is closely connected with a number of atoms, the simulations need to be large enough to mimic the bulkiness of the materials or at least have its effects minimized. The set rule for the simulations is that the x and y

lengths of the substrate need to be three times the diameter of the indenter, for the z-axis rule, was set during test simulations that displacements of atoms should reach the bottom layer which is used to fixate the substrate in order not to move down with the indentation. These rules were taken from previously published articles [16], also common neighbour analysis in Ovito was performed to see how far the dislocation spread. The simulation setup can be seen in fig. 4.3, where the comparison of indenter and substrate can be seen. The size of the substrate was set to  $200 \times 200 \text{ \AA}$  and the z-axis is always double the max indenter depth. The substrate was generated using the AtomsK program by using a unit cell from the Crystallographic website [17] for  $\alpha$  titanium and [18] for  $\beta$  titanium.

## 4.2 Indentor

Modelling of an indenter is another factor which contributes to simulation results. For the simulations three different shapes for indentors were chosen: spherical, conical and cylindrical. Fig. 4.2 shows the geometry and sizes of indentors. All indentors are generated by AtomsK with a diamond structure with a crystal parameter of  $a = 3.567 \text{ \AA}$ . As was mentioned in chap. 1, there are many indenter types used in real nanoindentation testing. During MD simulations more closer look at the indenter is taken, as is seen in fig. 4.2, the size of indenter used are in 10s of Angstroms. This means that the approximation between the experiment and real testing is only in spherical indenter since the real indenter used is never as sharp as indentors shown in fig. 4.2. These indentors in simulations are used to compare of using different

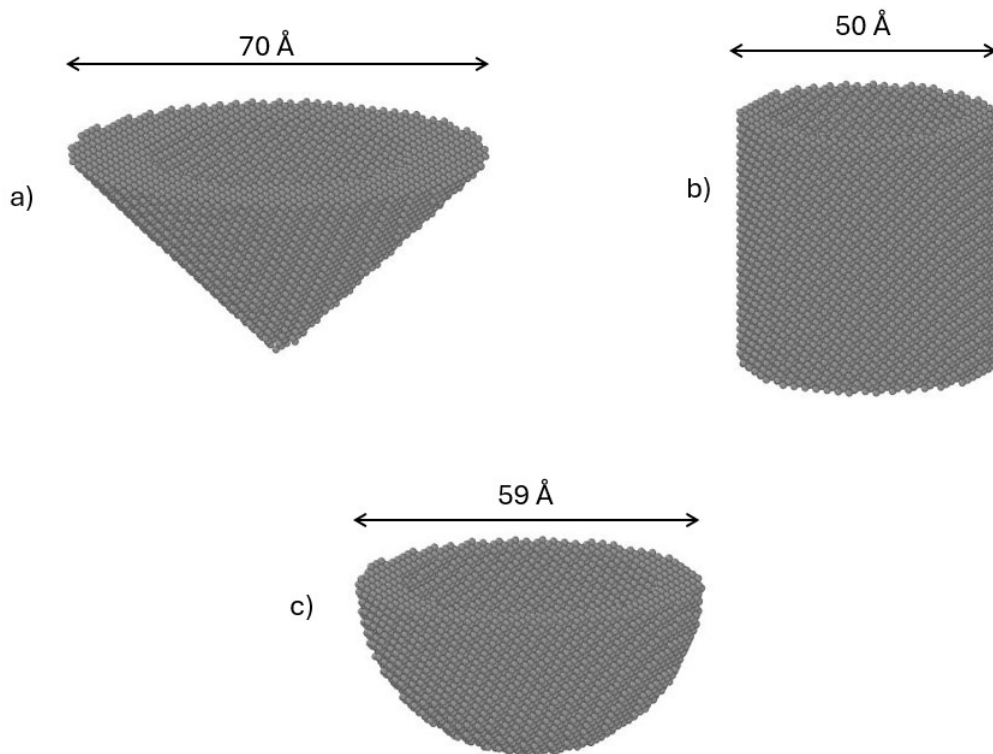


**Figure 4.2:** Figure shows indentors used during simulations with different shapes: a) conical, b) cylindrical and, c) spherical.

shapes of indentors, as chap. 3 states that different indenter shapes can be used in O&P’s approach. Modelling the indentors also contributes to computational time.

### 4.3 Simulation set up

As was mentioned previously simulations were done by Lammmps. The source code you can find in appx. A, where all the steps of the simulations and setup is described. Set-up contributes to accuracy and computational time. Simulation models assume periodic boundary conditions (pbc) along the x and y directions and along the z direction, non-periodic and shrinking boundary conditions are assumed. All mobile atoms in all simulations affected by the movement of the indenter follow Newtonian dynamics. As mentioned in the previous paragraph, layers underneath of substrate are fixed in order for the substrate not to move with the intended upon contact. In this simulation model, atoms in the indenter were kept fixed (the indenter was assumed to be an infinitely rigid body since the intent was to understand the mechanics of the substrate, not the indenter). All these are the following simulations performed in previous articles [19]. The temperature was set up to be 300 K where NVT thermostat was used to keep the temperature relatively the same.

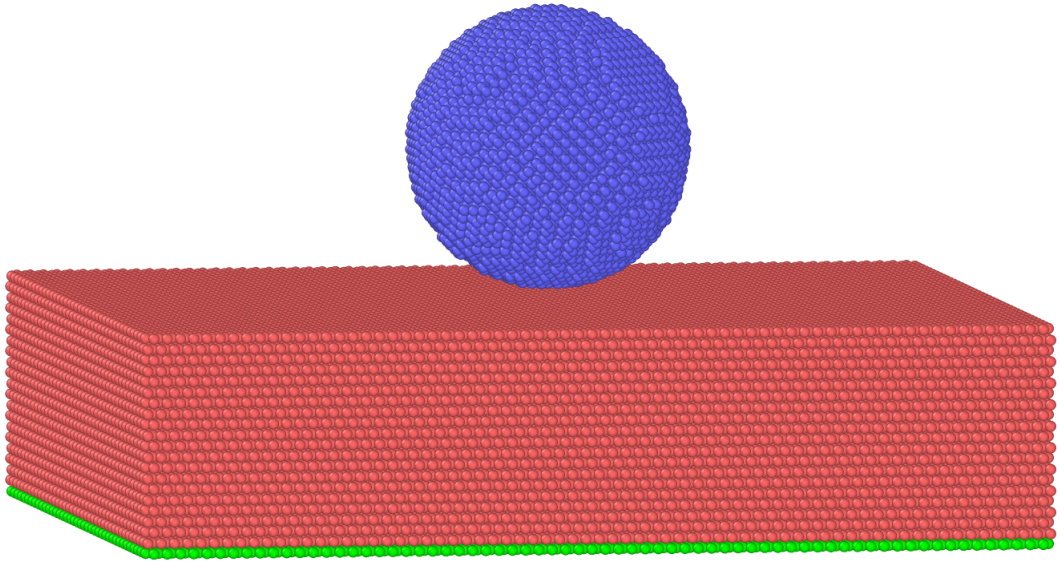


**Figure 4.3:** Figure showing simulation set up with spherical indenter (blue), Titanium substrate (red) and fixed bottom edge (green).

During all simulations, the same potential parameters were used to ensure the uniformity of the simulations. Two different potentials were used: for titanium eam potential from [20] was used and for carbon-titanium interaction, LJ potential with these parameters was used. The parameters for this potential were taken from [21], where the parameters  $\epsilon$  and  $\sigma$  are adopted as 3.14 meV and 3.722 meV. The cut-off distances for C-Ti are set as 0.6nm.

The last couple of parameters connected with simulations are about moving the indenter. The experimental technique is matured now and the results from it are accurate. The speed of the simulations is one of the general challenges when using MD simulations and it creates a bridge between the real experiments and simulations. The range of the speed was chosen from papers published [22] on similar topics where the speeds range from 10 m/s to 100 m/s. The next parameter connected with speed is the indentation depth, for this parameter the indenter was placed close to the surface and the distance was set between 4Å and 40Å.

# Chapter 5

## Results and discussion

This chapter organizes and details the results obtained, comparing them with existing literature. It is structured based on different stimulation sets, each focused on a specific simulation parameter. Initially, it presents findings related to parameters critical for calculation speed and accuracy, such as indentation depth and indenter velocity. These results lead to the use of various indentors, reflecting the theoretical assertion that practical nanoindentation techniques can accommodate multiple indenter types. Subsequent simulations identified optimal parameters, which were then selected based on computational efficiency to conduct simulations across different phases of titanium and various crystal orientations. Finally, one simulation was selected to be repeated three times using the same parameters to evaluate accuracy and identify potential errors.

### 5.1 Effect of indentation depth on simulations

The initial dataset presents an analysis of four distinct simulations, each characterized by varying distances that the indenter traveled during simulation  $h_{ind}$ , this changed also the final indentation depth. All parameters of the simulation are listed in the tab. 5.1. This variability was systematically introduced by maintaining a consistent indenter speed across simulations while adjusting the duration of each. This adjustment effectively elongates both the loading and unloading phases of the simulations. In fig. 5.1, the load-displacement data for each simulation run is shown. Together with fig. 5.2, there can be seen some phenomenons happening on an atomic level. Fig. 5.1, shows for 10Å sudden drop in indentation depth around 25 nN, marked

**Table 5.1:** Simulation parameters for a set of simulations showing the effect of indentation depth on simulations, where  $h_{ind}$  represents distances that the indenter travelled during simulation.

Material	Ti- $\alpha$	Ti- $\alpha$	Ti- $\alpha$	Ti- $\alpha$
$h_{ind}$ [Å]	5	10	15	20
Indentation speed [m/s]	0.1	0.1	0.1	0.1
Refraction speed [m/s]	0.1	0.1	0.1	0.1
Peak indentation force [nN]	248.54	288.89	211.95	225.42



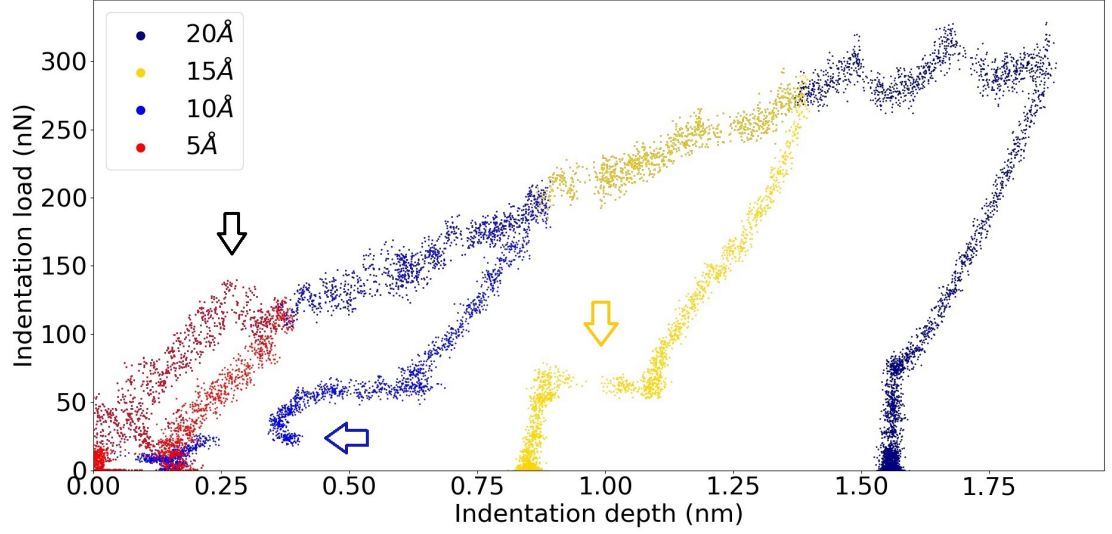


**Figure 5.1:** Figure shows load-displacement data for different  $h_{ind}$  as shown in the legend. The black arrow shows where the transition from elastic to plastic deformation starts. Blue and yellow arrows show atomic phenomena happening during simulations.

by blue arrow. After taking a look at the simulation and fig. 5.1, it is apparent that the drop is around  $1\text{\AA}$  which is around one atom layer. This is explained by the set-up of the simulation, which uses a dynamic group in Lammmps to monitor indentation depth. What can happen is that an atom can appear in the region and suddenly the indentation depth rises by one atom layer. This is due to the relaxation of the atoms.

After a closer look at fig. 5.2 displaying more behaviours observed across the different simulations. Initially, there is a phase of stabilization, where the substrate atoms exhibit considerable movement as they seek stability. This initial phase is critical as it explains why there is no significant movement from the indenter at the start of

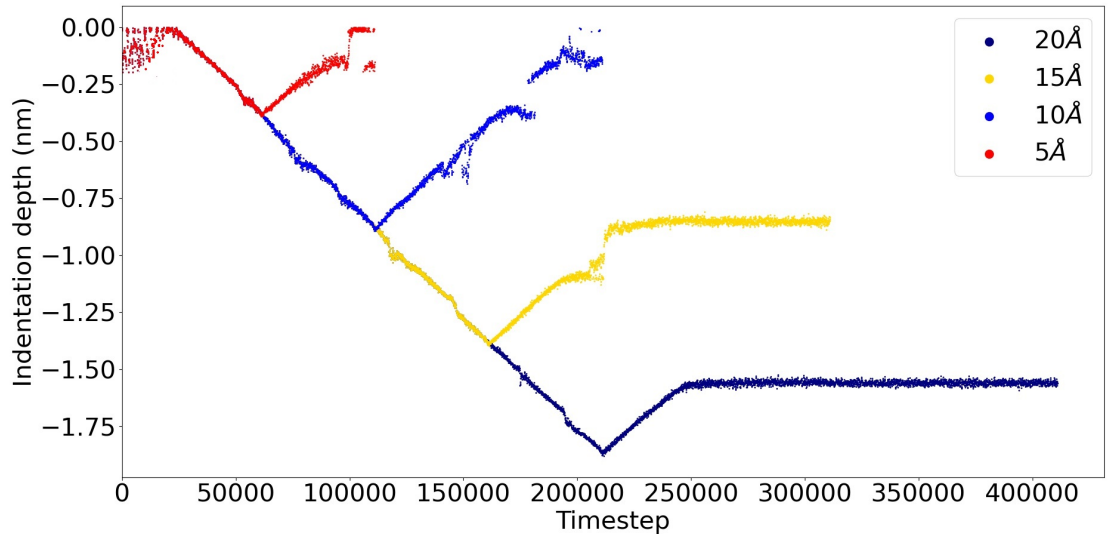


**Figure 5.2:** Figure shows time evolution of indenter depth for different  $h_{ind}$ .

the simulation. As the simulation progresses, a notable phenomenon occurs—a sharp increase in indentation depth by  $14\text{\AA}$  after 220 000 timesteps (in the fig. 5.2). This sudden change is a critical point of analysis, as it indicates a rapid rearrangement of atoms within the region of indentation. In some instances, atoms abruptly shift from the periphery towards the centre, resulting in a significant and rapid increase in indentation depth, observable within a few short timesteps. This is a similar effect as happened for simulation for  $10\text{\AA}$ , mentioned in the previous paragraph.

The graph in fig. 5.1 compiles all the load-displacement curves from the simulations. These curves feature sudden drops at the maximum load  $P_{max}$  (values can be seen in tab. 5.1), consistent with theoretical predictions discussed in chap. 3. These drops are significant as they indicate occurrences during the loading phase that are reflective of atomic failure mechanisms. According to previous research [14], such events are typically associated with dislocations, nucleation, and interactions between atoms.

One particularly important observation from the data is the first notable drop at 0.25 nm, signifying the transition from elastic to plastic deformation. This can be seen in fig. 5.1, marked with black arrow. This transition point is pivotal for understanding the material behaviour under stress and offers insights into the material’s mechanical properties and structural integrity under varying conditions of stress and strain. Such detailed analysis helps in enhancing our understanding of material behaviour at the microscopic level, paving the way for more refined simulations and improved predictive capabilities in materials science.

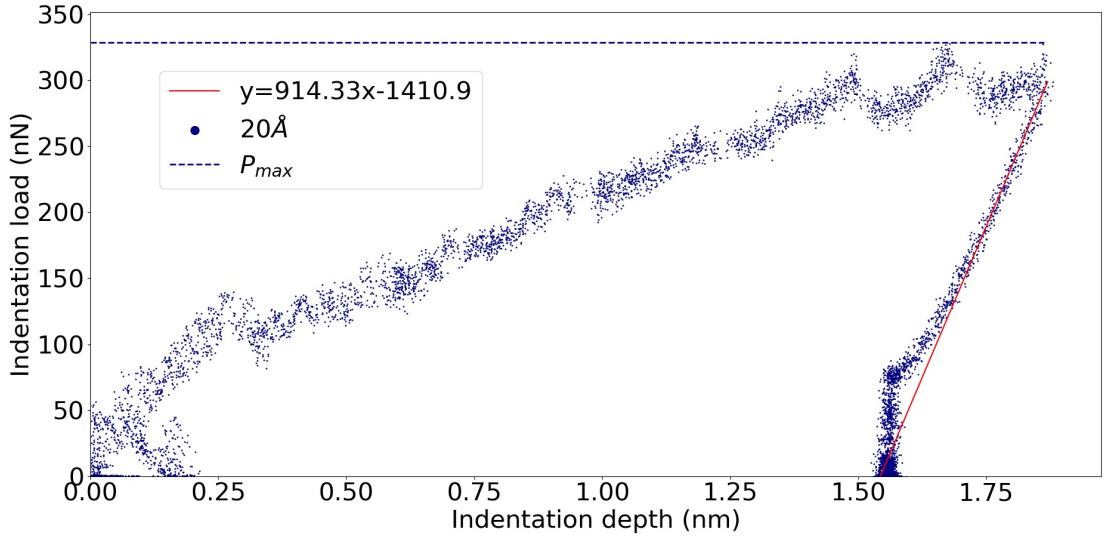


**Figure 5.3:** Figure shows load-displacement data for  $h_{ind} = 20\text{\AA}$ , with dotted line showing the maximum load  $P_{max}$ . The red line represents the fitted function used to calculate the stiffness of the material.

These datasets are utilized to derive values for hardness and Young’s modulus based on the theoretical framework outlined in chap. 3. In fig. 5.3 is shown analysis of load-displacement data. There is shown  $P_{max}$  for the dataset and also fitted linear function for unloading data which is used to determine stiffness  $S$ . These are used to determine the hardness and Young’s module as was mentioned in chap. 3. Calculations for each simulation are documented in the tab. 5.2.

The simulations can be divided into two kinds. For the first two, elastic behaviours can be seen. This is determined from the load-displacement graph shown in fig. 5.1. This can be seen in elastic behaviours since the curves are coming back to zero or close to zero. After a closer look at the simulation itself, we can check the indent after the unloading phase and it is apparent that the atoms for the 5Å have relaxed back to the original flat surface. The 10Å simulation has almost the same flat surface, there is only one atom layer which was removed. This shows small plastic deformation and such minimal indentation depth does not provide a robust basis for accurate measurements of hardness and Young’s modulus.

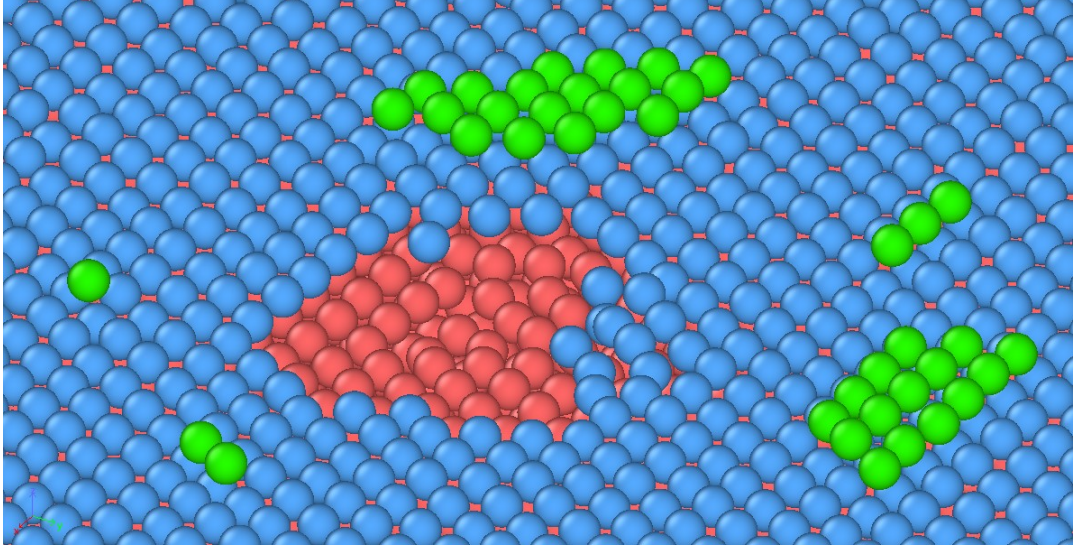


**Figure 5.4:** Figure shows the indent of simulation  $h_{ind} = 10\text{\AA}$ , where we can see three layers of atoms. The blue layer is the flat surface layer, the red layer is the atoms underneath and the green layer is the atoms on the flat surface, this indicates the simulation has some indent but is small enough not to be used for analysis.

On the other hand, the simulations with indentation depths of 14Å and 19Å exhibited significant drops post-maximum load, qualifying them for stiffness calculations as outlined in chap. 3. The outcomes are compiled in a tab. 5.2, highlighting that while Young’s modulus measurements across these simulations are relatively consistent, the hardness values vary notably with each depth. This variability in hardness can be attributed to the smaller indentation depths, which render the analyses more sensitive to changes in indentation depth and the abrupt increases noted previously at 14Å. In the tab. 5.2, also the values from literature are included, it can be seen that the simulations are not far off and when comparing the results from simulated results in papers, the results are satisfactory. These results can be improved by using

**Table 5.2:** Results of simulations for distances travelled by indenter between 4Å to 14Å, with comparison to measured value for bulk titan from literature [23].

	Simulations				Ref
$h_{max}$ [Å]	4	9	14	19	—
$H$ [GPa]	—	—	14.14	8.32	3.83 GPa
$E_r$ [GPa]	—	—	140.98	139.53	120.00 GPa

different potentials or using different parameters. One of which is velocity, explored in the next section.

Lastly, by using common neighbour analysis (used to determine the structure between the atoms), we can look at the structure's state after nanoindentation. Before the indenter moves, fig. 5.5 shows the structure of the substrate, where the red colour HCP structure dominates, and the surface atoms are marked as without any structure.

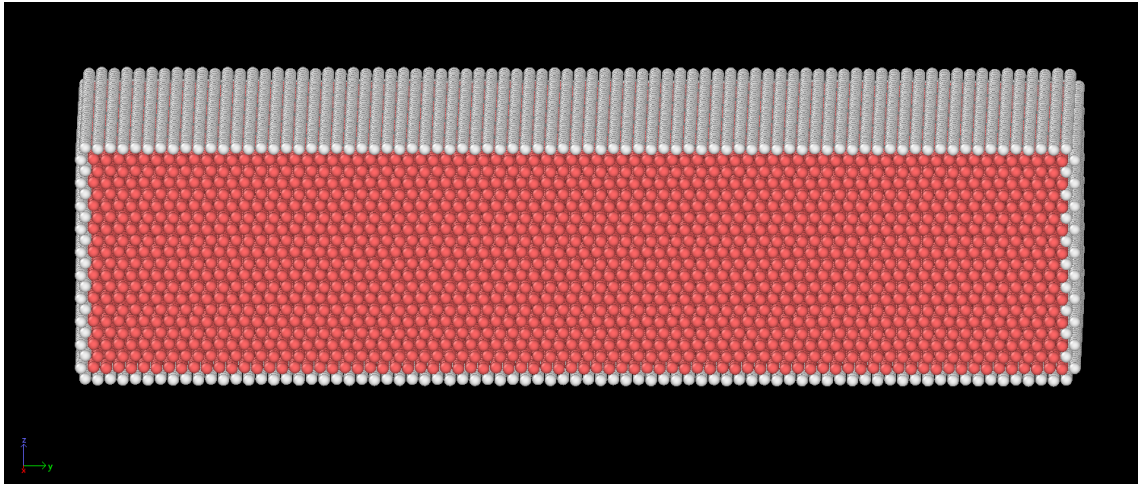


**Figure 5.5:** Figure showing the slice at  $100\text{\AA}$  in the x direction with common neighbour analysis performed. Red atoms mean HCP structure as is expected and grey atoms mean without structure, which is why all surface atoms are included here.

After nanoindentation and after removing the indenter from the simulation, in fig. 5.5, there can be seen the whole profile of the indent, we can see that almost all structures around the indent have relaxed back to the HCP structure. This ensures that the indent is permanent and that it is plastic deformation since there is no expected relaxation after the structure has formed. But when we turn the slice of the substrate by  $90^\circ$ . This gives us a view of some cluster of atoms inside of the

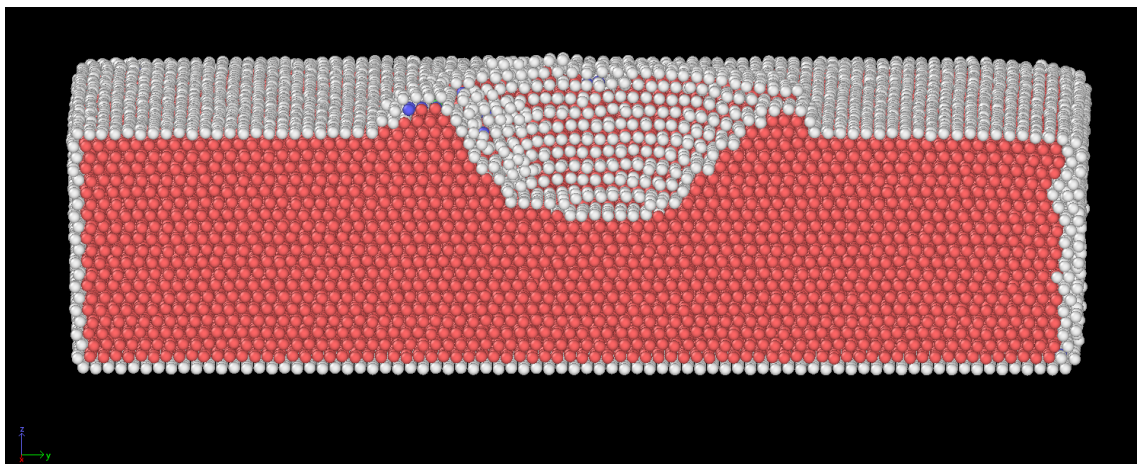


**Figure 5.6:** Figure showing the slice at  $100\text{\AA}$  in the x direction with common neighbour analysis performed, after nanoindentation. Red atoms mean HCP structure, blue atoms represent BCC structure and grey atoms mean without structure.

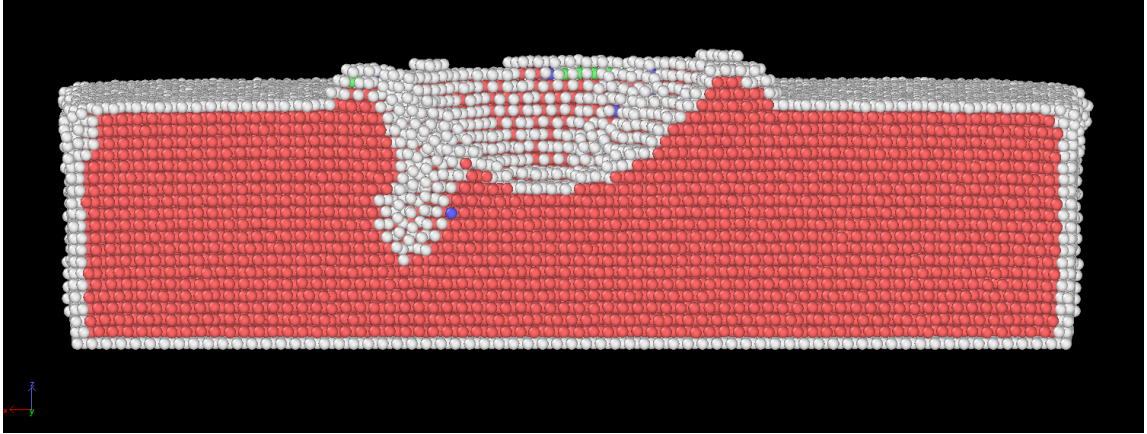


**Figure 5.7:** Figure showing the slice at  $100\text{\AA}$  in the  $y$  direction with common neighbour analysis performed, after nanoindentation. Red atoms mean HCP structure, blue atoms represent BCC structure and grey atoms mean without structure.

substrate which did not form the HCP structure. After going through different simulations performed during this study more of this phenomenon was found that the atoms in one direction have not formed the structure back to HCP but stayed unorganized. This is some form of a residue from the nanoindentation, during the period of maximum load the atoms are displaced in a circular shape in the direction of the negative  $z$ -axis. This creates a small hollow cylinder of displaced atoms surrounded by structural HCP atoms. This can be observed in the fig. 5.8, where HCP atoms

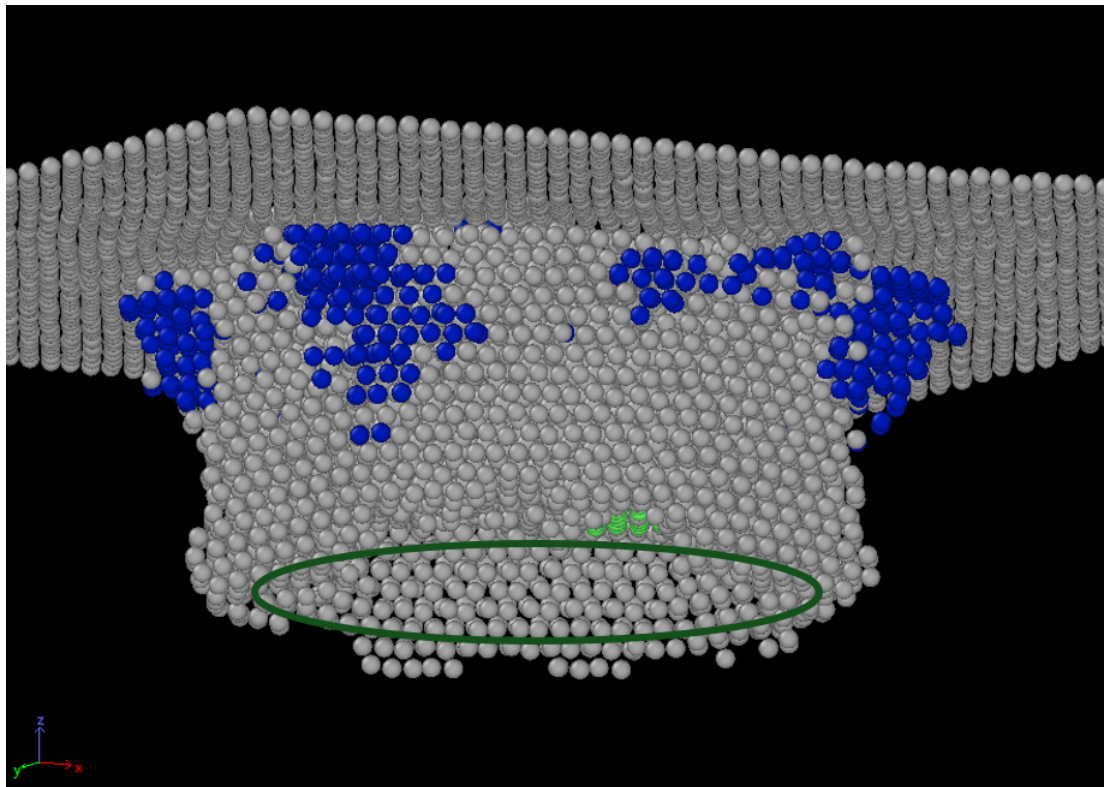


**Figure 5.8:** Figure showing the structure of the substrate after removing HCP atoms and leaving only BCC (blue), FCC (light green) and unorganized (grey). A green circle is used to visualize how the profile of unorganized atoms looks from below.

were removed and only BCC, FCC and unorganized atoms were kept. There also can be seen outline and the mentioned cylinder when the green circle is used to help visualise it. When comparing the result to the literature, the formation of this hollow cylindrical shape is something unusual, the literature suggests that the atom's dislocations and displacements keep close to the indent and surround it [5]. This can be further studied, to see if this is a recurring theme or something unusual.

## 5.2 Analysis of simulation precision and stability

This section is used to analyze the stability and precision of the performed simulations in the previous set. The chosen run was with  $h_{ind}$  set to 20Å and it was performed 4 times back to back, with no change to parameters. Parameters can be seen in the tab. 5.3.

**Table 5.3:** Simulation parameters for a set of simulations showing the precision and stability of the performed simulations.

Material	Ti- $\alpha$
$h_{ind}$ [Å]	20
Indentation speed [m/s]	0.3
Refraction speed [m/s]	0.3
Average peak indentation force [nN]	356.98

The results of the repeated simulation confirm the precision and stability of the performed simulations. The first graph in the fig. 5.9, shown completely overlapping data for each of the runs. This is also confirmed by the second graph where we see that the final indentation depth is at the same level and data is also overlapping. The results of these repeated runs are shown in the tab. 5.4, where it can be seen that the runs produced for hardness have almost the same values and don't differ. Young's module seems to be more susceptible to change even in repeated runs, which means that this precision needs to be taken into consideration when working with values calculated by MD simulations.

**Table 5.4:** Results of simulations for repeated runs.

run number	1	2	3	4
$H$ [GPa]	12.76	12.78	12.12	12.51
$E_r$ [GPa]	109.76	107.54	130.58	115.93

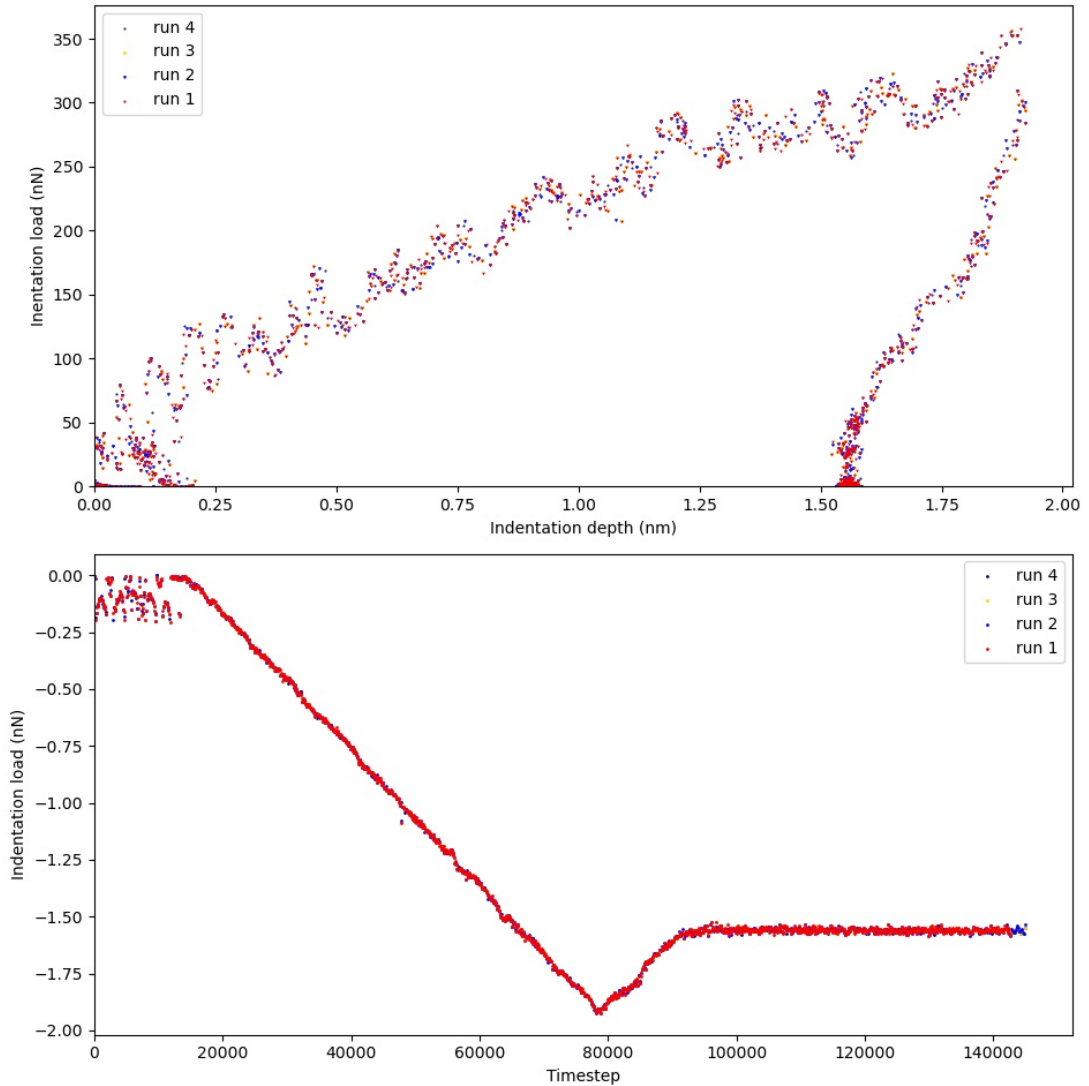


**Figure 5.9:** The figure consists of two graphs illustrating the outcomes of the repeated simulation sets. The first graph presents load-displacement data, specifically load versus indentation depth, where all four simulations are overlaying each other. The second graph plots indentation depth against timestep, charting the progression of indentation depth and displaying the various final and maximum indentation depths observed in the simulations.



### 5.3 Effect of indentation velocity on simulations

The next set of simulations delved into assessing the impact of varying indenter speeds on calculated values of hardness and Young’s modulus. Five distinct speeds ranging from 10 m/s to 50 m/s were selected for these simulations and all parameters can be found in tab. 5.5. The corresponding indentation depth evolution and load-displacement data are illustrated in fig. 5.10. Analysis of the indenter depth evolution reveals that the final depth reached by the indenter was consistent across all five simulations. Additionally, the overlapping nature of the load-displacement data sets suggests that speed changes do not significantly influence the outcomes for hardness and Young’s modulus. There can be seen a slight increase of  $P_{max}$ , which is expected since with higher velocity the force acting on the indenter is expected to increase.

**Table 5.5:** Parameters of simulations showing the effect of indenter velocity on simulations.

Material	Ti- $\alpha$	Ti- $\alpha$	Ti- $\alpha$	Ti- $\alpha$	Ti- $\alpha$
Indentation speed [m/s]	10	20	30	40	50
Refraction speed [m/s]	10	20	30	40	50
Peak indentation force [nN]	328.63	327.51	358.25	368.35	375.77

The second graph in fig. 5.10, there are also found some atomic phenomenons. First, there is the stabilization of the substrate at the beginning where atoms create a jump in an indentation depth as they are stabilizing (masked by green arrow in fig. 5.10). The next phenomenon (marked by the black arrow in fig. 5.10) is caused by atom movement and simulation set-up as was mentioned in the previous section. When atom’s natural thermal movement causes the atom to pass to the region where indentation depth is measured. The last phenomenon is marked by the red arrow and is caused by atom movement, when the indenter is pushing down atoms sometimes an atom with its natural movement can move in the same direction which causes this small ripple.

The analytical approach employed in the previous simulation sets was similarly applied here, with results displayed in tab. 5.6. The calculated hardness values ranged between 8.19 GPa and 12.56 GPa, whereas Young’s modulus ranged from 117.86 GPa to 142.71 GPa. The average values calculated were 10.12 GPa for hardness and 127.25 GPa for Young’s modulus, indicating that individual results closely align with the average values.

These findings corroborate the initial hypothesis that the speed of indentation does

**Table 5.6:** Results of simulations for different indenter speeds between 10 m/s and 50 m/s.

	Simulations					Ref
$v$ [m/s]	10	20	30	40	50	—
$H$ [GPa]	11.5	9.5	11.4	11.8	12.6	3.8 GPa
$E_r$ [GPa]	121.8	124.6	130.6	117.9	142.7	120 GPa

not materially affect the measurements of hardness and Young's modulus, aligning with conclusions drawn in previous research [22]. This consistency across different speeds underscores the robustness of the hardness and Young's modulus measurements against variations in operational conditions within the tested range.

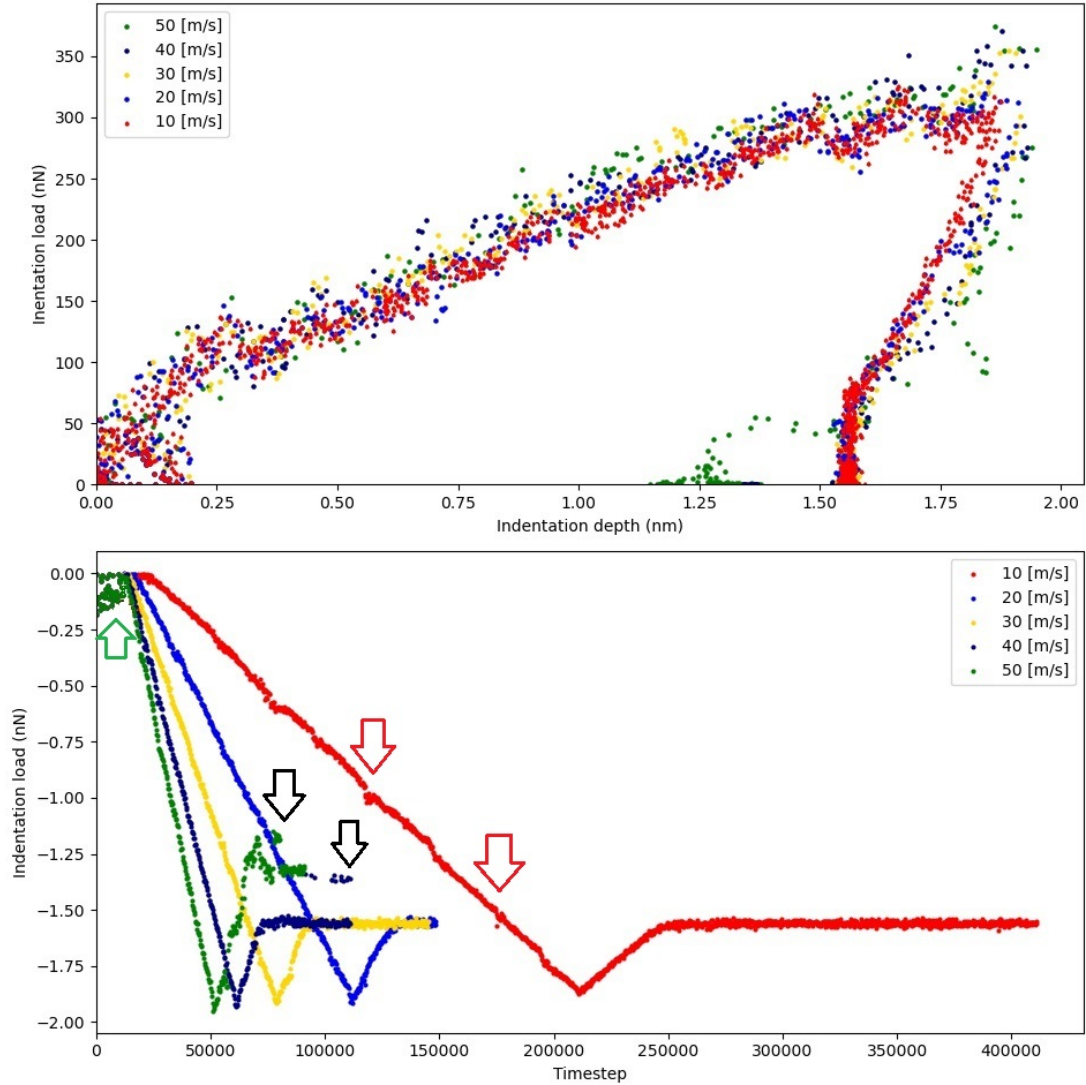


**Figure 5.10:** The figure consists of two graphs illustrating the outcomes of the second simulation sets, differentiated by various indenter velocities as indicated in the legend in the first graph. The first graph presents load-displacement data, specifically load versus indentation depth, where all five simulations are overlaying each other. The second graph plots indentation depth against timestep, charting the progression of indentation depth and displaying the various final and maximum indentation depths observed in the simulations. Arrows in the second graph represent different atomic phenomena happening in simulations, caused by atomic thermal movement.

## 5.4 Different indentors simulations

The forthcoming simulations are to evaluate three distinct types of indentors: spherical, conical, and cylindrical as was discussed in chap. 4. Parameters used in these simulations are listed in tab.5.7. Detailed analysis as was performed in previous sections, was conducted for each simulation, with findings presented in tab. 5.8. Since the previous section revealed that velocity has little to no effect on the result, a speed of 30 m/s was chosen to shorten the computational time.

**Table 5.7:** Parameters of simulations showing the effect of different indenter types.

Material	Ti- $\alpha$	Ti- $\alpha$	Ti- $\alpha$
Indentation speed [m/s]	30	30	30
Refraction speed [m/s]	30	30	30
Peak indentation force [nN]	328.63	327.51	358.25

The results indicate that the spherical indenter is the most effective for these simulations, followed closely by the cylindrical indenter. Conversely, the conical indenter yielded the least favourable outcomes. A detailed examination of the indentation simulations revealed a significantly larger relaxation effect with the conical indenter compared to the others. This phenomenon is evident from the final indentation depth of 9.73Å, which is substantial considering the maximum indentation depth was 50.7Å. The pronounced relaxation can be attributed to the acuteness of the conical indenter, which facilitates easier atomic displacement back towards the original crystal structure.

**Table 5.8:** Results of simulations for different indenter shapes using the velocity of 30 m/s and indentation depth of 50Å and referential values [23]..

Indenter type	Simulations			Ref
	spherical	conical	cylindrical	
$H$ [GPa]	8.19	36.09	15.38	3.83 GPa
$E_r$ [GPa]	120.55	271.35	141.60	120 GPa

## 5.5 Different crystal orientations simulations

In our most recent set of simulations, optimal parameters were selected from prior experiments, prioritizing both performance and computational efficiency. The specific setup utilized a spherical indenter propelled at a velocity of 30 m/s and achieved an indentation depth of approximately 29 angstroms. These parameters can be seen also in tab. 5.9. These results are systematically presented in tab. 5.10.

**Table 5.9:** Parameters of simulations showing the effect of different crystal orientations and phases.

Material	Ti- $\alpha$ <100>	Ti- $\alpha$ <110>	Ti- $\alpha$ <111>	Ti- $\beta$ <100>
Indentation speed [m/s]	30	30	30	30
Refraction speed [m/s]	30	30	30	30
Peak indentation force [nN]	428.36	427.15	458.54	421.13

The comparative analysis between alpha and beta titanium revealed an expected outcome: beta titanium displayed a lower hardness compared to alpha titanium. This observation agrees with the literature since the hardness of  $\beta$  titanium is averaging at 2.5 GPa [24]. The values are not matching with the literature but the trend between the phases of decreasing hardness is kept. This suggests that the simulations are not precise enough to get a closer value than 6.92 GPa but they are keeping the lowering with changing phase which suggests that simulations are stable. This can be improved by using different potentials or increasing the simulations in a number of atoms.

**Table 5.10:** Results of simulations for crystal orientations for each titanium phase, where the velocity of 30 m/s with a depth of 29Å.

Sample	Ti- $\alpha$ <100>	Ti- $\alpha$ <110>	Ti- $\alpha$ <111>	Ti- $\beta$ <100>
$H$ [GPa]	9.58	8.87	7.88	6.92
$E_r$ [GPa]	125.48	114.65	116.24	125.02

Additionally, the effect of crystallographic orientation on material hardness was assessed. The data indicate a negligible influence of orientation on the overall hardness, with a notable exception in the <111> orientation, where a slight decrease in hardness was observed. According to the referenced literature [25], this phenomenon can be attributed to increased atomic spacing in this orientation, which facilitates greater deformability and subsequent lattice restructuring in the deformation layer. Results from this simulation set are to be taken with caution since the chosen orientations are not significant for hexagonal structures. Exploring other orientations is advised since, for example, to take some orientation suggested from this paper [26].

It is essential to approach all results with caution. The minor variations observed across different simulation runs could reflect inherent inaccuracies in the simulation methodology, potentially stemming from the chosen computational potential or the parameters utilized. Such discrepancies highlight the need for careful consideration of simulation settings and their potential impact on the accuracy and reliability of the results. As was mentioned previously the simulations are not precise enough

to get values similar to values provided by the literature. For our simulations the number of atoms used is around 140 000 (depending on the used indenter) if this number had been increased to 1 million this might improve the values of hardness and Young's module.

# Conclusion

In this work, we have systematically dissected the complex interactions between indenter speed, and indentation depth, and used the experience to apply it to determining the optimal crystal orientation for titanium. Our examination spanned a variety of scenarios, from initial depth-specific simulations to assessments across different indenter speeds and shapes, providing a comprehensive view of material responses at the microscopic level.

The comprehensive analyses conducted across a series of simulations provide significant insights into the atomic behaviour of materials under varying conditions of indentation mechanics. The series of simulations detailed in this discussion have offered significant insights into the atomic behaviour of materials under varying conditions of indentation depth, indenter velocity, and indenter shape. The analyses reveal that the hardness and Young's modulus measurements remain relatively consistent with changes in velocity, specifically noting that speeds ranging from 10 m/s to 50 m/s produced hardness values between 9.45 GPa and 12.56 GPa and Young's modulus values from 117.86 GPa to 142.71 GPa. Also, analysis of data for different indentation depths revealed the limit of 10Å in order for the analysis to become viable for further material analysis. These findings are essential for validating the robustness of the computational models used and suggest that the simulation parameters chosen do not significantly affect the outcome within the tested ranges. The exploration of different indenter shapes introduced another layer of complexity. The spherical and cylindrical indentors generally performed better in maintaining consistent indentation depths and mechanical properties, whereas the conical indentors showed a significant relaxation effect, potentially due to their shape facilitating easier atomic displacement. This part of the study highlights the importance of indenter geometry in determining the outcomes of such simulations. One set of simulations was also performed to see the repetitiveness and stability of the simulations, where all the results from the same simulations repeated 4 times gave almost the same values for hardness, Young's module have a tendency to diverge a bit more but is still in a range of 10% accuracy.

Lastly, the examination of the difference in hardness between  $\alpha$ -titanium and  $\beta$ -titanium phase reveals and confirms the literature's tendency for  $\beta$ -titanium to have lower hardness than  $\alpha$ -titanium. For the different crystal orientations ( $\langle 100 \rangle$ ,  $\langle 110 \rangle$ ,  $\langle 111 \rangle$ ) in  $\alpha$ -titanium phase, it reveals that while material properties generally remain consistent across different orientations, there are subtle differences that could be crucial for applications requiring more precise material simulations. Also, the choice of other orientations could bring more interesting results.

Overall, the findings of this research align well with the existing body of knowledge.

Looking forward, refining simulation parameters, such as enlarging the substrate size and enhancing computational efficiency, could improve the outcomes. Exploring additional crystal orientations or incorporating polycrystalline structures could provide deeper insights. Moreover, aspects not yet examined in this study, like using different computational potentials and broadening the scope to include other materials, could further increase the precision and relevance of our results.

# Bibliography

1. HTV-MEMBERSHIP. *Nanoindentation* [online]. 2024. [visited on 2024-04-29]. Available from: [https://www.htv-gmbh.de/wp-content/uploads/2023/08/Analytik\\_Nanoindenter-EN-1-250x341-1.jpg](https://www.htv-gmbh.de/wp-content/uploads/2023/08/Analytik_Nanoindenter-EN-1-250x341-1.jpg).
2. OLIVER, W.C.; PHARR, G.M. An improved technique for determining hardness and elastic modulus using load and displacement sensing indentation experiments. *Journal of Materials Research*. 1992, vol. 7, no. 6, pp. 1564–1583. Available from DOI: 10.1557/JMR.1992.1564.
3. HERTZ, Heinrich. Ueber die Berührung fester elastischer Körper. *Journal für die reine und angewandte Mathematik*. 1882, vol. 1882, no. 92, pp. 156–171. Available from DOI: doi:10.1515/crll.1882.92.156.
4. FISCHER-CRIPPS, A.C. *Nanoindentation*. Springer New York, 2013. Mechanical Engineering Series. ISBN 9780387224626. Available also from: <https://books.google.se/books?id=pnzlBwAAQBAJ>.
5. YU, Ning; POLYCARPOU, Andreas. Use of the focused ion beam technique to produce a sharp spherical diamond indenter for sub-10 nm nanoindentation measurements. *Journal of Vacuum Science Technology B: Microelectronics and Nanometer Structures*. 2004, vol. 22. Available from DOI: 10.1116/1.1676467.
6. LEE, June Gunn. *Computational materials science: an introduction*. CRC press, 2016.
7. I. NEZBEDA J. Kolafa, M. Kotrla. *Úvod do molekulárních simulací Metody Monte Carlo a molekulární dynamiky*. Karolinum, 2002. ISBN 9788024606491.
8. MILLER, F.P.; VANDOME, A.F.; JOHN, M.B. *Lennard-Jones Potential*. VDM Publishing, 2010. ISBN 9786132689559. Available also from: <https://books.google.cz/books?id=sE9ZXwAACAAJ>.
9. DAW, Murray S.; BASKES, M. I. Embedded-atom method: Derivation and application to impurities, surfaces, and other defects in metals. *Phys. Rev. B*. 1984, vol. 29, pp. 6443–6453. Available from DOI: 10.1103/PhysRevB.29.6443.
10. SNEDDON, Ian N. Boussinesq's problem for a rigid cone. *Mathematical Proceedings of the Cambridge Philosophical Society*. 1948, vol. 44, no. 4, pp. 492–507. Available from DOI: 10.1017/S0305004100024518.



11. THOMPSON, A. P.; AKTULGA, H. M.; BERGER, R.; BOLINTINEANU, D. S.; BROWN, W. M.; CROZIER, P. S.; 'T VELD, P. J. in; KOHLMAYER, A.; MOORE, S. G.; NGUYEN, T. D.; SHAN, R.; STEVENS, M. J.; TRANCHIDA, J.; TROTT, C.; PLIMPTON, S. J. LAMMPS - a flexible simulation tool for particle-based materials modeling at the atomic, meso, and continuum scales. *Comp. Phys. Comm.* 2022, vol. 271, p. 108171. Available from DOI: [10.1016/j.cpc.2021.108171](https://doi.org/10.1016/j.cpc.2021.108171).
12. STUKOWSKI, Alexander. Visualization and analysis of atomistic simulation data with OVITO-the Open Visualization Tool. *MODELLING AND SIMULATION IN MATERIALS SCIENCE AND ENGINEERING*. 2010, vol. 18, no. 1. ISSN 0965-0393. Available from DOI: [10.1088/0965-0393/18/1/015012](https://doi.org/10.1088/0965-0393/18/1/015012).
13. HIREL, Pierre. AtomsK: A tool for manipulating and converting atomic data files. *Computer Physics Communications*. 2015, vol. 197, pp. 212–219. ISSN 0010-4655. Available from DOI: <https://doi.org/10.1016/j.cpc.2015.07.012>.
14. MA, Bin; RAO, Qiu-hua; HE, Yue-hui. Effect of crystal orientation on tensile mechanical properties of single-crystal tungsten nanowire. *Transactions of Nonferrous Metals Society of China*. 2014, vol. 24, no. 9, pp. 2904–2910. ISSN 1003-6326. Available from DOI: [https://doi.org/10.1016/S1003-6326\(14\)63425-7](https://doi.org/10.1016/S1003-6326(14)63425-7).
15. LIMITED, Hebei Metals Industrial. *The Crystal Structure of Titanium* [online]. 2024. [visited on 2024-04-29]. Available from: <http://www.metalspiping.com/wp-content/uploads/2018/07/crystal-structure-of-%CE%B1-ti-hcp-and-%CE%B2-ti-bcc.jpg>.
16. GOEL, Saurav; JOSHI, Suhas S.; ABDELAL, Gasser; AGRAWAL, Anupam. Molecular dynamics simulation of nanoindentation of Fe<sub>3</sub>C and Fe<sub>4</sub>C. *Materials Science and Engineering: A*. 2014, vol. 597, pp. 331–341. ISSN 0921-5093. Available from DOI: <https://doi.org/10.1016/j.msea.2013.12.091>.
17. HULL, A. W. Crystal structure of titanium, zirconium, cerium, thorium and osmium. *Physical Review*. 1921, vol. 18, pp. 88–89.
18. BALLOR, JoAnn; POPLAWSKY, Jonathan D.; DEVARAJ, Arun; MISTURE, Scott; BOEHLERT, Carl J. Lattice Parameter Evolution during the Beta-to-Alpha and Beta-to-Omega Transformations of Iron- and Aluminum-Modified. *Crystals*. 2024, vol. 14. ISSN 2073-4352. Available from DOI: [10.3390/cryst14020145](https://doi.org/10.3390/cryst14020145).
19. VERKHOVTSEV, Alexey V.; YAKUBOVICH, Alexander V.; SUSHKO, Genady B.; HANAUSKE, Matthias; SOLOV'YOV, Andrey V. Molecular dynamics simulations of the nanoindentation process of titanium crystal. *Computational Materials Science*. 2013, vol. 76, pp. 20–26. ISSN 0927-0256. Available from DOI: <https://doi.org/10.1016/j.commatsci.2013.02.015>.
20. MENDELEV, M. I.; UNDERWOOD, T. L.; ACKLAND, G. J. Development of an interatomic potential for the simulation of defects, plasticity, and phase transformations in titanium. *The Journal of Chemical Physics*. 2016, vol. 145, no. 15, p. 154102. ISSN 0021-9606. Available from DOI: [10.1063/1.4964654](https://doi.org/10.1063/1.4964654).

21. FU, Tao; PENG, Xianghe; ZHAO, Yinbo; SUN, Rong; WENG, Shayuan; FENG, Chao; WANG, Zhongchang. Molecular dynamics simulation of TiN (001) thin films under indentation. *Ceramics International*. 2015, vol. 41, no. 10, Part B, pp. 14078–14086. ISSN 0272-8842. Available from DOI: <https://doi.org/10.1016/j.ceramint.2015.07.027>.
22. XU, Shuai; WAN, Qiang; SHA, Z.D.; LIU, Zishun. Molecular dynamics simulations of nano-indentation and wear of the Ti-Al alloy. *Computational Materials Science*. 2015, vol. 110, pp. 247–253. Available from DOI: [10.1016/j.commatsci.2015.08.045](https://doi.org/10.1016/j.commatsci.2015.08.045).
23. PELLETIER, H; KRIER, J; CORNET, A; MILLE, P. Limits of using bilinear stress–strain curve for finite element modeling of nanoindentation response on bulk materials. *Thin Solid Films*. 2000, vol. 379, no. 1, pp. 147–155. ISSN 0040-6090. Available from DOI: [https://doi.org/10.1016/S0040-6090\(00\)01559-5](https://doi.org/10.1016/S0040-6090(00)01559-5).
24. HERNANDEZ, J.; LI, S.J.; MARTINEZ, E.; MURR, L.E.; PAN, X.M.; AMATO, K.N.; CHENG, X.Y.; YANG, F.; TERRAZAS, C.A.; GAYTAN, S.M.; HAO, Y.L.; YANG, R.; MEDINA, F.; WICKER, R.B. Microstructures and Hardness Properties for  $\beta$ -Phase Ti–24Nb–4Zr–7.9Sn Alloy Fabricated by Electron Beam Melting. *Journal of Materials Science Technology*. 2013, vol. 29, no. 11, pp. 1011–1017. ISSN 1005-0302. Available from DOI: <https://doi.org/10.1016/j.jmst.2013.08.023>.
25. ZHAO, Hongwei; ZHANG, Peng; SHI, Chengli; LIU, Chuang; HAN, Lei; CHENG, Hongbing; REN, Luquan. Molecular Dynamics Simulation of the Crystal Orientation and Temperature Influences in the Hardness on Monocrystalline Silicon. *Journal of Nanomaterials*. 2014, vol. 2014, pp. 1–8. Available from DOI: [10.1155/2014/365642](https://doi.org/10.1155/2014/365642).
26. MERSON, E; BRYDSON, R; BROWN, A. The effect of crystallographic orientation on the mechanical properties of titanium. *Journal of Physics: Conference Series*. 2008, vol. 126, no. 1, p. 012020. Available from DOI: [10.1088/1742-6596/126/1/012020](https://doi.org/10.1088/1742-6596/126/1/012020).
27. *LAMMPS Documentation*. 2024. <https://docs.lammps.org/Manual.html>.

# Appendix

## A LAMMPS source code

This section describes the used LAMMPS source code. All the commands are explained more in detail in official documentation [27]. With this code, there are also secondary files needed such as the simulation atom file which was generated in AtomsK and described in chap. 4 and potential files from [20]. The code is divided into two parts shown sequentially in fig. 11 and 12.

The first block of the code, shown in fig. 11, is used to set changing parameters in simulations, such as indenter velocity, number of steps and timestep. All of these are used to modify and reconfigure parameters as they are needed in the code and simulation. There are 5 important parameters, indenter speed (line 6) which together with timestep and `run_steps` determine the indenter depth of the simulation. There is also the `minimize_steps` (line 7) parameter which is used to minimize and stabilize the substrate before the indentation.

The second block of the code is called system generation. This part defines dimensions, and boundary conditions (lines 15 and 16) as mentioned in chap. 4, also specify units (line 17) used throughout the code, these units can be found here [27]. The neighbour commands (lines 19 and 20) are used to set up the build of the simulation and affect the cutoff distance for force reach during the simulation.

The third block of code is used to define the first region of the simulation and create the box (lines 25 and 26). This is the initial set-up of the space where the simulations will be running. After the region is set up, the read of the simulation atom file for substrate and indenter is needed (line 27), as mentioned in chap. 4.

After all the atoms used in the simulation are read, the third block of the code is used to set up all the different groups and regions required for the successful simulation to happen. There is first a need to divide atoms into two groups to separate substrate (`mobile + lower_edge`) and indenter (`indenter_group`), where the substrate is further divided into atom layer at the bottom (`lower_fix`). The bottom layer is then substrates to create a mobile substrate group (`mobile`). The last part is to create a group in a certain region (line 38), including only atoms from the substrate to use in monitoring the indentation depth. This group is set up to be dynamic in order to monitor only the region not the atoms which are assigned to it, so the atoms will be monitored as they enter the region.

The last part from the first fig. 11, is the potential set-up, where `hybrid pair_style` potential defines the types of potentials used. The first potential used is for Ti-

```

1
2
3 # Parameters to be changed for simulations
4 timestep 0.001
5 variable shape equal "sphere"
6 variable vel_ind equal "0.3"
7 variable stabilization_steps_1 equal "10000"
8 variable run_steps_in equal "67000"
9 variable stabilize_steps_2 equal "1000"
10 variable run_steps_out equal "67000"
11 variable vel_ind_minus equal "-v_vel_ind"
12
13
14 # system generation
15 dimension 3
16 boundary p p s
17 units metal
18 atom_style atomic
19 neighbor 0.3 bin
20 neigh_modify delay 5
21 atom_modify map yes
22
23
24 # create geometry and import structure
25 region box_1 block -300 300 -300 300 -500 500
26 create_box 2 box_1
27 read_data materials/Ti_Dia_sphere.lmp add append group substrate
28
29
30 # Create all groups and regions necessary
31 region indenter block INF INF INF INF 48 INF
32 group indenter_group region indenter
33 region lower_fix block INF INF INF INF INF 2.25
34 group lower_edge region lower_fix
35 # if any other fixed atoms are required they can be added here
36 group not_mobile union lower_edge
37 variable atom_type atom type==1
38 region depth block 100 104 103 107 INF 48
39 group depth_group dynamic all region depth var atom_type every 1
40 group mobile subtract all indenter_group not_mobile
41 displace_atoms indenter_group move 0 0 1 units box
42
43
44 # Set up potential
45 pair_style hybrid eam/fs lj/cut 8.5
46 pair_coeff * * eam/fs Ti1.eam.fs Ti Ti
47 pair_coeff 1 2 lj/cut 0.00314 3.7588 6
48

```

**Figure 11:** Figure showing the first part of the code, which is divided into 5 blocks.

Ti interaction as mentioned in chap. 4 for each interaction. Then we change the interaction Ti-C to Lj potential also mentioned in chap. 4.

The second part of the code is shown in fig. 12, where the code is divided into 4 blocks. The first block is used to set up the simulation from the physics point of view. First worth mentioning is to set up indenter\_group group as a system of microcanonical ensemble (NVE) (line 55) and for mobile group system is set up as canonical (NVT), where start and stop temperature was set to 300 K, this also works as a thermostat to keep the temperature around 300K. This code block also fixes atom groups for the indenter and bottom layer of the substrate as mentioned in chap. 4.

```

49
50 # set up simulations enviroment
51 compute      peratom all pe/atom
52 compute      new mobile temp
53 velocity     mobile create 300 482748 temp new
54 thermo       500
55 thermo_modify temp new
56 fix          02 indenter_group setforce 0.0 0.0 0.0
57 fix          1 indenter_group nve
58 fix          01 mobile nvt temp 300.0 300.0 $(100.0*dt)
59 fix          2 not_mobile setforce 0.0 0.0 0.0
60
61
62 # COMPUTE
63 # force on the intendor
64 compute force_ft mobile      force/tally indenter_group c_force_ft
65 # indentation depth of indendor
66 compute z indenter_group      reduce      min z
67 # indentation depth of specimen
68 compute z1 depth_group        reduce      max z
69
70
71 # ALL DUMPS
72 fix      0001      all          ave/time 1 1 50 c_z c_z1 c_force_ft file dumps/data.txt
73 dump     peratom   all          custom 250  dumps/sim.dump      id type x y z
74 dump     2         depth_group  custom 250  dumps/sim_vpich.dump id type x y z
75
76
77 # RUN steps
78 # stabilization
79 run      $(v_stabilization_steps_1)
80 # move indenter down
81 variable V equal v_vel_ind_minus
82 variable z equal vdisplace(0.0,$V)
83 fix      001 indenter_group move variable NULL NULL v_z NULL NULL v_V
84 run      $(v_run_steps_in)
85 unfix    001
86 # wait
87 fix      001 indenter_group move variable NULL NULL NULL NULL NULL NULL
88 run      $(v_stabilize_steps_2)
89 # move indenter up
90 variable V equal v_vel_ind
91 variable z equal vdisplace(0.0,$V)
92 fix      001 indenter_group move variable NULL NULL v_z NULL NULL v_V
93 run      $(v_run_steps_out)
94

```

**Figure 12:** Figure showing the second part of the code, which is divided into 4 blocks.

The next block of code in fig. 12, computes necessary values with each timestep for later analysis, line 64 is used to compute the force between the indenter and substrate used as an indenter load in the analysis. Line 66 computes the minimal atom position for the indenter group to monitor indenter movements and line 68 computes the maximum from depth\_group which is used as an actual indenter depth.

The third block fig. 12, is used to set up the necessary dumps needed for later analysis. The first sump in line 72 is used to collect calculated values from the previous paragraph and save it with every 50 timesteps. The second two dumps save the atom's position from all atoms and depth\_group to have the possibility to see the atom's behaviours.

The last part of the code is the actual set-up of the runs, which is divided into 4 different runs. Here, the parameters from the first block are used to set up the indenter speed and run steps. The first run is used to stabilize the substrate before the nanoindentation starts. The next three parts are the actual nanoindentation, where in lines 83 and 92 speed is assigned to the indenter group, where the speed is defined in previous lines.